Topological frequency conversion in Weyl semimetals

Frederik Nathan[1,2], Ivar Martin[3], Gil Refael[1]
[1] *Department of Physics and Institute for Quantum Information and Matter, California Institute of Technology, Pasadena, California 91125, USA*
[2] *Center for Quantum Devices, Niels Bohr Institute, University of Copenhagen, 2100 Copenhagen, Denmark*
[3] *Material Science Division, Argonne National Laboratory, Argonne, IL 60439, USA*
(Dated: February 1, 2022)

We show that a Weyl semimetal irradiated at two distinct frequencies can convert energy between the frequencies at a potentially large rate. The phenomenon is a realization of topological frequency conversion from [Martin *et al*, PRX **7** 041008 (2017)]. When the effect is realized, each electron near a Weyl point acts as a topological frequency converter, and converts energy at a universal rate given by Planck's constant multiplied by the product of the two frequencies. Our results indicate that Weyl points in TaAs support topological frequency conversion in the THz regime and at achievable intensities of order $100\mathrm{W/mm}^2$. When the topological energy conversion rate exceeds the dissipation rate, the effect can be used for optical amplification. This amplification regime can be achieved when the relaxation rate of the system is larger than the characteristic driving period. This phenomenon further amplifies Weyl semimetals' promise for optical amplification and terahertz (THz) generation.

Weyl semimetals are at the center of topological materials research thanks to their rich phenomenology [1–12] and promising technological applications [13–15]. They are characterized by topologically protected nodes in the band structure near the Fermi surface that give rise to (pseudo)spin-momentum locked low-energy excitations with linear dispersion. Being surrounded by very high Berry curvature, these nodal points, or Weyl points, lead to unusual linear and nonlinear optical properties which make Weyl semimetals promising platforms for, e.g., photovoltaics and high-harmonic generation [15–23].

In recent years, it was also appreciated that the interplay between external driving and band topology can give rise to a rich variety of exotic phenomena [24–30]. Particularly relevant for our work, *bichromatic* driving (i.e., simultaneous driving at two distinct frequencies) can induce topological phenomena even in zero-dimensional systems: Ref. [31] showed that a spin driven by two oscillating magnetic fields with incommensurate frequencies f_1 and f_2 can enter a regime where it transfers energy between the driving modes at a universal average rate given by the "energy transfer quantum", hf_1f_2, where h denotes Planck's constant. This effect was termed topological frequency conversion. Related phenomena with the same universal rate of energy transfer were also discussed in Refs. [32–34].

While the model from Ref. [31] has been experimentally implemented and studied [35, 36], actual observation of topological frequency conversion is still lacking. The reasons are two fold: First, in the magnetic realm, topological frequency conversion in the desirable frequency regime of THz and above requires extremely high amplitudes of the oscillating magnetic field (of about 1 Tesla and above, corresponding to radiation intensities of more than $240\,\mathrm{MW/mm}^2$). Even then, measurable – and especially *useful* – conversion rates would require many spins acting synchronously.

In this work we propose a Weyl semimetal as the medium of choice for realizing topological frequency conversion at high frequencies and with large conversion rates. For that we consider a Weyl semimetal, subjected to incoming radiation at two incommensurate frequencies, as depicted in Fig. 1(a). Under appropriate driving, individual electrons near the Weyl nodes act as an ensemble of topological frequency converters (as in Ref. 31), with the (pseudo-)spin of each electron playing the role of the spin, and the vector potential potential playing the role of the magnetic field (the "transduction" being provided by the Fermi velocity of the Weyl point). As a result, the system hosts and ensemble of electrons that each convert energy from mode 2 to mode 1 at the quan-

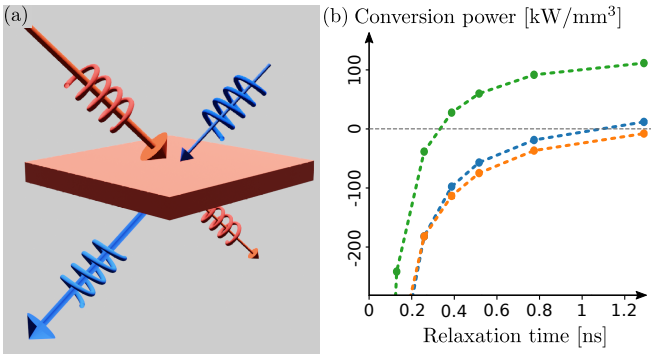

FIG. 1. (a) Schematic illustration topological frequency conversion. When irradiated by electromagnetic modes with distinct angles and frequencies (blue and red) a Weyl semimetal (orange), can transfer energy from one mode to the other. (b) The numerically calculated transfer rate per unit volume, η, as a function of relaxation time τ, for an isolated Weyl node with Fermi velocity $3.87 \cdot 10^5\mathrm{m/s}$. Here modes 1 and 2 has intensities $2.14\,\mathrm{kW/mm}^2$ and $8.57\,\mathrm{kW/mm}^2$, respectively, while mode 2 has frequency $f_2 = 1.23\,\mathrm{THz}$, and mode 1 has frequency $f_1 = (\sqrt{5}-1)f_2/2$, (blue), $f_1 = 2f_2/3$ (green), and $f_1 = 2f_2/(3+0.001\pi)$ (orange). See main text for further details of the model and the calculation.

tized rate $\pm hf_1f_2$ per electron.

Notably, in Weyl semimetals, the strong coupling needed to achieve topological frequency conversion does not require extremely large radiation intensity. That is because the effective spins interact directly with electric field the via vector potential rather than with the magnetic field. In this way, we find that Weyl points in known compounds (such as TaAs) begin support THz conversion at radiation intensities above $\sim 100\,\mathrm{W/mm^2}$.

Under favorable conditions, conversion power can be quite large: at Terahertz frequencies, and intensities of $\mathrm{kW/mm^2}$, our analytical estimates and simulations indicate the conversion power per unit volume can be of order $100\,\mathrm{kW/mm^3}$ [see Eq. (30) and Fig. 1(b)].

Electronic relaxation processes, however, counteract the frequency conversion by providing a channel for trivial energy dissipation – material heating. For parameters corresponding to realistic band structures, we find that net energy gain of the pumped mode becomes possible for a characteristic relaxation time of order 1 nanosecond at THz frequencies [see Fig. 1(b)]. Such relaxation times are longer than the relaxation times of order $0.25\,\mathrm{ps} - 3\,\mathrm{ps}$ that have been mostly reported experimentally to date [37–40], although some experiments report signatures with much longer lifetimes [41, 42] that can even exceed 1 nanosecond [43].

Nonetheless, we expect slower relaxation rates can be achieved through improvement of materials quality and bath/substrate engineering. Additionally, excessive heating can be countered through pulsed driving, by allowing the system to dissipate away heat between the pulses.

The rest of this paper is structured as follows: in Sec. I we review the characteristic properties of Weyl semimetals, which forms the basis for our discussion. In Sec. II, we present the mechanism for frequency conversion from a single-particle perspective. Sec. III shows how topological frequency conversion arises in a realistic many-body system, taking into account the effects of finite frequency and dissipation. In Sec. IV, we support our conclusions with numerical simulations. In Sec. V, we summarize the conditions that a Weyl semimetal and driving modes must satisfy to allow for topological frequency conversion. We conclude with a general discussion in Sec. VI. Details of derivations are provided in Appendices.

I. REVIEW OF WEYL SEMIMETALS

We begin by reviewing the characteristic properties of Weyl semimetals. This review forms the basis for our subsequent discussion.

Weyl semimetals are 3-dimensional materials in which two adjacent energy bands touch at isolated points in the Brillouin zone [11, 12], as depicted in Fig. 2(a). These band-touching points are known as Weyl points. To understand Weyl points better, we consider the Bloch Hamiltonian of the system, $H(\mathbf{k})$, near one such Weyl point, which we (without loss of generality) take to be located at wave vector $\mathbf{k} = 0$. When restricted to the subspace spanned by the two touching bands, and linearized in $\mathbf{k}$ around $\mathbf{k} = 0$, $H(\mathbf{k})$ takes the following characteristic form:

$$H(\mathbf{k}) = \varepsilon_0 + \hbar \sum_{i,j} \sigma_i R_{ij} k_j + \hbar \sum_i V_i k_i + \mathcal{O}(\mathbf{k}^2), \quad (1)$$

where σ_x, σ_y and σ_z denote the Pauli matrices acting on the subspace spanned by the two touching bands in some given basis, R is a real-valued symmetric full-rank 3×3 matrix, while $\mathbf{V} = (V_1, V_2, V_3)$ and ε_0 is a real-valued velocity and energy, respectively. Evidently, the two energy bands of $H(\mathbf{k})$ included above touch at the Weyl point ($\mathbf{k} = 0$). When the touching energy bands are plotted in the plane $k_i = 0$ (for $i = x, y,$ or z), the bands form a characteristic "touching cones" structure, as for example in Fig. 2(a). ε_0 determines the location of the touching point on the energy axis, while $\mathbf{V}$ determines the "tilt" of the cones. The eigenvectors and spectrum of R determines the anisotropy (or "squeezing") of the band gap around the Weyl point.

Once it is present, a Weyl point is a very robust feature: as long R remains full-rank, any infinitesimal perturbation to the system can only shift the location of the band-touching point, but not eliminate it. This is straightforward to verify through direct calculation. Hence, a smooth change of system parameters can only cause Weyl points to continuously move around in the Brillouin zone [44]. As a result of this robustness, Weyl semimetals are a generic class of materials. Indeed, many materials have recently been shown to be Weyl semimetals [10–12, 45–51].

Another novel feature of Weyl semimetals is the nontrivial band topology associated with the eigenstates of the Bloch Hamiltonian, $\{|\psi_\alpha(\mathbf{k})\rangle\}$. These topological properties are captured by the Berry curvature $\mathbf{\Omega}_\alpha(\mathbf{k}) = (\Omega^1_\alpha(\mathbf{k}), \Omega^2_\alpha(\mathbf{k}), \Omega^3_\alpha(\mathbf{k}))$ where

$$\Omega^i_\alpha(\mathbf{k}) = i \sum_{j,k=1}^{3} \epsilon_{ijk} \langle \partial_j \psi_\alpha(\mathbf{k}) | \partial_k \psi_\alpha(\mathbf{k}) \rangle, \quad (2)$$

with ϵ_{ijk} denoting the Levi-Civita tensor and ∂_i the partial derivative with respect to the ith component of crystal wave vector, k_i (we discuss the physical significance of the Berry curvature below). Weyl points act as point sources for Berry curvature: for two bands, 1 and 2, touching at an isolated Weyl node at $\mathbf{k} = \mathbf{k}_i$, the Berry curvature of the upper band, 2, satisfies

$$\nabla \cdot \mathbf{\Omega}_2(\mathbf{k}) = 2\pi\, \mathrm{sgn}(|R|) \delta(\mathbf{k} - \mathbf{k}_i), \quad (3)$$

were $|\cdot|$ denotes the determinant, and ∇ the nabla operator in $\mathbf{k}$-space. The sign is reversed for the the lower band. The relationship between Weyl points and Berry curvature is in exact analogy to point charges and the electric field. In this analogy, the index $q \equiv \mathrm{sgn}|R|$ determines the "charge", or chirality, of the Weyl point [52]. The net charge of all Weyl points that appear within a

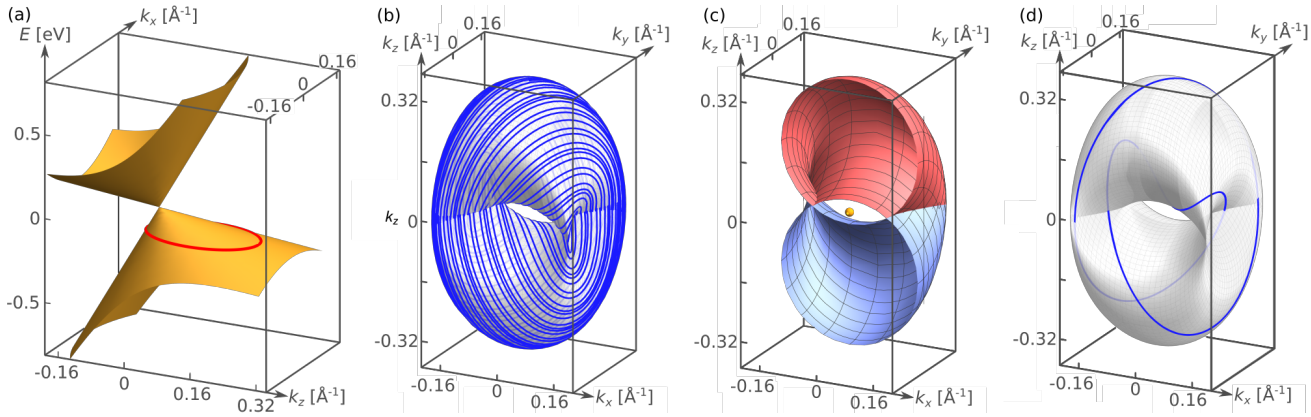

FIG. 2. (a): Energy bands of the linearized Hamiltonian in Eq. (1) in the plane $k_y = 0$, with $\varepsilon_0 = 0$, $R_{ij} = \delta_{ij} 3.87 \cdot 10^5$ m/s, and $\mathbf{v} = (0, 0, 3.1 \cdot 10^5 \text{m/s})$. The red line shows an example of the Fermi surface (with Fermi energy -115 meV) when projected into the same plane. (b): Trajectory of $e\mathbf{A}(t)/\hbar$ resulting from two modes with circular polarization in the xz and yz planes with amplitudes $\mathcal{E}_1 = 0.74\,\text{MV/m}$, $\mathcal{E}_2 = 1\,\text{MV/m}$ and frequencies, $f_2 = 1, \text{THz}$, $f_1 = \frac{\sqrt{5}-1}{2} f_2$ (blue). Also shown is the surface $\mathcal{B}_0$ (gray). See main text for further details. (c): Cross-section of $\mathcal{B}_0$ for the same parameters as in (b). Within the red and blue sub-surfaces $W(\mathbf{k})$ takes value 1 and -1, respectively, while $W(\mathbf{k}) = 0$ outside the surface. (d): Trajectory of $e\mathbf{A}(t)/\hbar$ for the same values of $\mathcal{E}_2$ and f_2 as in (b), and with $E_1 = 0.72\,\text{MV/m}$, $f_1 = \frac{2}{3} f_2$ (resulting in a commenusrate frequency ratio). The different value of $\mathcal{E}_1$ is chosen to ensure that the vector potential of mode 1 has the same amplitude in panels (b) and (d), such that the topological phase boundary $\mathcal{B}_0$ is the same for panels (b-d).

given gap is zero [1]; thus any gap must hold an even number of Weyl points.

For a system with many bands and multiple Weyl points, Eq. (3) generalizes to

$$\nabla \cdot \mathbf{\Omega}_\alpha = 2\pi \sum_i q_i s_{i,\alpha} \delta(\mathbf{k} - \mathbf{k}_i), \tag{4}$$

where the sum runs over all Weyl points in the system, q_i denotes the chirality of Weyl point i, and $s_{i,\alpha}$ indicates how the Weyl points of the system connect the bands: specifically $s_{i,\alpha} = 1$ if Weyl point i connects band α with the adjacent band above, $s_{i,\alpha} = -1$ if it connects band α with the band below, and $s_{i,\alpha} = 0$ if band α is not involved at Weyl point i.

Eq. (4) can equivalently be expressed using the divergence theorem: for a closed surface in the Brillouin zone, $\mathcal{C}$, the total Berry flux of band α, $\oint_\mathcal{C} \mathrm{d}^2\mathbf{S} \cdot \mathbf{\Omega}_\alpha(\mathbf{k})$ (which is identical to the Chern number of band α when constricted to the 2-dimensional closed surface $\mathcal{C}$), is given by $\sum_{\mathbf{k}_i \in \mathcal{C}} q_i s_{\alpha,i}$ where the sum runs over all Weyl points contained within $\mathcal{C}$.

Berry curvature acts as a magnetic field in reciprocal space: an electron in band α with a relatively well-defined position and wavevector, $\mathbf{r}$ and $\mathbf{k}$, acquires a transverse velocity proportional to $\mathbf{\Omega}_\alpha(\mathbf{k})$ when subject to a weak external force [53], $\dot{\mathbf{k}}$:

$$\dot{\mathbf{r}}_\alpha(\mathbf{k}) = \frac{1}{\hbar} \nabla_\mathbf{k} \varepsilon_\alpha(\mathbf{k}) + \dot{\mathbf{k}} \times \mathbf{\Omega}_\alpha(\mathbf{k}). \tag{5}$$

This second term above is known as *anomalous velocity*, and can be seen as a canonically-conjugate analog to the Lorentz force: whereas a magnetic field $\mathbf{B}$ generates a velocity in reciprocal space perpendicular to the real-space velocity, $\dot{\mathbf{k}} = -\frac{e}{\hbar}\mathbf{B} \times \dot{\mathbf{r}}$ (the Lorentz force), Berry curvature generates a real-space velocity perpendicular to the reciprocal space velocity, $\dot{\mathbf{r}} = \dot{\mathbf{k}} \times \mathbf{\Omega}_n$ (the anomalous velocity); here e denotes the elementary charge.

Eq. (3) implies that the Berry curvature diverges near Weyl points. Hence electrons with wavevectors near a Weyl point experience a divergent anomalous velocity [54]. When subject to an applied electric field, $\mathbf{E}$, such that $\dot{\mathbf{k}} = -e\mathbf{E}/\hbar$, Weyl semimetals can thus produce a large current response which may be nonlinear as a function of $\mathbf{E}$. This significant nonlinearity makes Weyl materials particularly attractive as nonlinear optical media, with potential applications including high-harmonic generation, frequency conversion and photovoltaics [15, 19].

In principle, any material the band geometry that has large local Berry curvature near the Fermi level is prone to having strong nonlinear response; Weyl semimetals are just a prominent example of those thanks to the divergent Berry curvature near the Weyl points. However, this is not the full story: the exotic band *topology* of Weyl semimetals (i.e. the nontrivial winding of the Berry curvature around Weyl points) in itself gives rise to unique nonlinear response phenomena. The effect we explore in this paper – topological frequency conversion – is an example of such an inherently topological response phenomenon.

II. FREQUENCY CONVERSION FROM A SINGLE ELECTRON

Here we show how the nontrivial band topology of Weyl semimetals allows electrons to act as topological

frequency converters [31, 55]. We consider a Weyl semimetal irradiated by two electromagnetic waves, or "modes", with distinct propagation angles and frequencies, and with elliptical or circular polarization. Fig. 1(a) depicts a concrete example in which the two waves are circularly polarized in the xz and yz planes. We let $\mathbf{E}_1(t)$ and $\mathbf{E}_2(t)$ denote the electric fields resulting from mode 1 and 2, respectively, such that the net electric field in the Weyl semimetal at time t is given by $\mathbf{E}(t) = \mathbf{E}_1(t)+\mathbf{E}_2(t)$. We assume the wavelengths of the incoming waves to be much longer than the relevant length scales we consider, and hence take $\mathbf{E}_i(t)$ to be spatially uniform. The two modes are oscillating with frequencies f_1 and f_2, such that, for $i = 1, 2$, $\mathbf{E}_i(t) = \mathbf{E}_i(t + T_i)$, where $T_i \equiv 1/f_i$. For simplicity, we first consider the case where f_1 and f_2 are incommensurate; we consider the case of commensurate frequencies in Sec. II A.

The coupling between the Weyl semimetal and the electromagnetic radiation is captured by the Peierls substitution [56], which causes the driven system to be governed by the time-dependent Bloch Hamiltonian

$$H(\mathbf{k}, t) = H(\mathbf{k} + e\mathbf{A}(t)/\hbar), \tag{6}$$

where $\mathbf{A}(t) = \int_0^t \mathrm{d}s\, \mathbf{E}(s)$ denotes vector potential induced by $\mathbf{E}(t)$ [57]. In the following $H(\mathbf{k})$ denotes the Hamiltonian of the system in the absence of the driving, while $H(\mathbf{k}, t)$ denotes the Hamiltonian in the presence of the driving.

It is useful to decompose the vector potential as $\mathbf{A}(t) = \mathbf{A}_1(t) + \mathbf{A}_2(t)$, where $\partial_t \mathbf{A}_i(t) = \mathbf{E}_i(t)$. Since $\mathbf{E}_i(t)$ is generated by electromagnetic radiation, its time-average vanishes; hence $\mathbf{A}_i(t)$ is also T_i-periodic with respect to t. Without loss of generality we take both $\mathbf{A}_1(t)$ and $\mathbf{A}_2(t)$ to have time-average zero (recall that constant shifts in $\mathbf{A}(t)$ correspond to benign gauge transformations). It is convenient to represent the vector potentials $\mathbf{A}$ and $\mathbf{A}_i$ as explicit functions of the phases of the two modes , $\boldsymbol{\alpha}$ and $\boldsymbol{\alpha}_i$ (rather than single time variable). Specifically, $\boldsymbol{\alpha}(\phi_1, \phi_2) \equiv \mathbf{A}_1(\phi_1/\omega_1) + \mathbf{A}_2(\phi_2/\omega_2)$ and $\boldsymbol{\alpha}_i(\phi_i) \equiv \mathbf{A}_i(\phi_i/\omega_i)$, where $\omega_i \equiv 2\pi f_i$ denotes the angular frequency of mode i. We similarly let $\boldsymbol{\epsilon}(\phi_1, \phi_2)$ and $\boldsymbol{\epsilon}_i(\phi_i)$ denote the electric fields $\mathbf{E}$ and $\mathbf{E}_i$ as functions of the individual phases the two modes.

To reveal how topological frequency conversion emerges, we consider the dynamics of a single electron in band α, in a wavepacket with some relatively well-defined position, $\mathbf{r}$, and wavevector, $\mathbf{k}$. The rate of energy transferred to mode 1 by the wavepacket, $P_\alpha(\mathbf{k}, t)$, is given by Ohm's law [58],

$$P_\alpha(\mathbf{k}, t) = -e\mathbf{E}_1(t) \cdot \dot{\mathbf{r}}_\alpha(\mathbf{k}, t). \tag{7}$$

where $\dot{\mathbf{r}}_\alpha(\mathbf{k}, t)$ denotes the velocity of the wavepacket in band α at wavevector $\mathbf{k}$, given the Hamiltonian $H(\mathbf{k}, t)$. When ω_1 and ω_2 are small enough so that the time-dependence of $H(\mathbf{k}, t)$ is adiabatic [59], $\dot{\mathbf{r}}_\alpha(\mathbf{k}, t)$ is given by Eq. (5), with the instantaneous reciprocal space velocity given by $\dot{\mathbf{k}}(t) = -e\mathbf{E}(t)/\hbar$:

$$\dot{\mathbf{r}}_\alpha(\mathbf{k}, t) = \frac{1}{\hbar}\nabla_{\mathbf{k}}\varepsilon_\alpha(\mathbf{k}+e\mathbf{A}(t)) - \frac{e}{\hbar}\mathbf{E}(t)\times\boldsymbol{\Omega}_\alpha(\mathbf{k}+e\mathbf{A}(t)/\hbar). \tag{8}$$

Our goal is to compute the time-averaged rate of energy transfer into mode 1,

$$\bar{P}_\alpha(\mathbf{k}) \equiv \lim_{t\to\infty} \frac{1}{t}\int_0^t \mathrm{d}s\, P_\alpha(\mathbf{k}, s). \tag{9}$$

Here and throughout this work, we use the $\bar{\cdot}$ accent to indicate time-averaging, such that, for any function of time and, possibly, other parameters $f(t, x)$, $\bar{f}(x) \equiv \lim_{t\to\infty} \frac{1}{t}\int_0^t ds f(s, x)$.

To compute $\bar{P}_\alpha(\mathbf{k})$, we express $\dot{\mathbf{r}}_\alpha(\mathbf{k}, t)$ as a direct function of ϕ_1 and ϕ_2: $\dot{\mathbf{r}}_\alpha(\mathbf{k}, t) = \mathbf{v}_\alpha(\mathbf{k}; \omega_1 t, \omega_2 t)$. Here $\mathbf{v}_\alpha(\mathbf{k}; \phi_1, \phi_2)$ is obtained from the expression for $\dot{\mathbf{r}}_\alpha(\mathbf{k}, t)$ in Eq. (8) after replacing $\mathbf{A}(t)$ and $\mathbf{E}(t)$ with $\boldsymbol{\alpha}(\phi_1, \phi_2)$ and $\boldsymbol{\epsilon}(\phi_1, \phi_2)$, respectively. Since we assume ω_1 and ω_2 to be incommensurate, the time-averaged value of $\mathbf{E}_1(t) \cdot \dot{\mathbf{r}}_\alpha(\mathbf{k}, t)$ is identical to the phase-averaged value of $\boldsymbol{\epsilon}_1(\phi_1) \cdot \mathbf{v}_\alpha(\mathbf{k}; \phi_1, \phi_2)$. Hence,

$$\bar{P}_\alpha(\mathbf{k}) = \frac{-e}{4\pi^2}\int_0^{2\pi} \mathrm{d}\phi_1 \mathrm{d}\phi_2\, \boldsymbol{\epsilon}_1(\phi_1) \cdot \mathbf{v}_\alpha(\mathbf{k}; \phi_1, \phi_2). \tag{10}$$

Using the expression for $\mathbf{v}$ we described above, along with $\boldsymbol{\epsilon}_i = 2\pi f_i \partial_{\phi_i}\boldsymbol{\alpha}$, we obtain

$$\bar{P}_\alpha(\mathbf{k}) = f_1 f_2 \frac{e^2}{\hbar}\int_0^{2\pi} \mathrm{d}\phi_1 \mathrm{d}\phi_2\, (\partial_{\phi_1}\boldsymbol{\alpha}\times\partial_{\phi_2}\boldsymbol{\alpha})\cdot\boldsymbol{\Omega}_\alpha(\mathbf{k}-e\boldsymbol{\alpha}/\hbar). \tag{11}$$

See Appendix A for detailed derivation. The integral above has a direct geometrical interpretation: $\frac{e^2}{\hbar^2}\mathrm{d}\phi_1\mathrm{d}\phi_2\, (\partial_{\phi_1}\boldsymbol{\alpha} \times \partial_{\phi_2}\boldsymbol{\alpha})$ gives the differential area element of the closed surface defined by $e\boldsymbol{\alpha}(\phi_1, \phi_2)/\hbar$ in reciprocal space,

$$\mathcal{B}_0 \equiv \{e\boldsymbol{\alpha}(\phi_1, \phi_2)/\hbar\}, \quad 0 \le \phi_1, \phi_2 < 2\pi, \tag{12}$$

The direction of the differential area element $(\partial_{\phi_1}\boldsymbol{\alpha} \times \partial_{\phi_2}\boldsymbol{\alpha})$ defines the orientation of $\mathcal{B}_0$. In Fig. 2(b) we depict $\mathcal{B}_0$ for the case where modes 1 and 2 are circularly polarized in the xz and yz planes respectively, and have electric field amplitudes $\mathcal{E}_2 = 1\,\mathrm{MV/m}$, $\mathcal{E}_1 = 0.74\mathrm{MV/m}$, and frequencies $f_2 = 1\,\mathrm{THz}$, $f_1 = \frac{\sqrt{5}-1}{2} f_2$. For incommensurate frequencies, the trajectory of $e\mathbf{A}(t)/\hbar$ fills out $\mathcal{B}_0$ completely at long times, as also illustrated in Fig. 2(b).

With the above geometric interpretation, we find

$$\bar{P}_\alpha(\mathbf{k}) = f_1 f_2 \hbar \oint_{\mathcal{B}_0} \mathrm{d}^2\mathbf{k}' \cdot \boldsymbol{\Omega}_\alpha(\mathbf{k} + \mathbf{k}'), \tag{13}$$

where $\oint_{\mathcal{B}_0} \mathrm{d}^2\mathbf{k}'$ denotes the surface integral of $\mathbf{k}'$ over the surface $\mathcal{B}_0$. From Sec. I we recall that this integral is quantized as 2π times the net charge of Weyl points of band α enclosed within the surface $\mathcal{B}_0$ after displacing it by $\mathbf{k}$ from the origin in reciprocal space, $Q_\alpha[\mathbf{k}]$ (here

the enclosed charge is weighted by the orientation of $\mathcal{B}_0$ with respect to the volume in which the Weyl point is enclosed):

$$\bar{P}_\alpha(\mathbf{k}) = h f_1 f_2 Q_\alpha[\mathbf{k}] \tag{14}$$

where we used $h = 2\pi\hbar$.

For an isolated Weyl point with charge +1 located at $\mathbf{k} = 0$ in a two-band system, $Q_\alpha[\mathbf{k}]$ is given by the following for the upper band ($\alpha = 2$):

$$Q_2[\mathbf{k}] = -W(\mathbf{k}), \tag{15}$$

where the function $W(\mathbf{k})$ is integer-valued and denotes the net winding number of $\mathcal{B}_0$ around $\mathbf{k}$ as a function of ϕ_1 and ϕ_2. In Fig. 2(c) we plot $W(\mathbf{k})$ for the configuration of two circularly polarized modes also considered in Fig. 2(b). The sign is reversed for mode 2 [i.e., when replacing $\mathbf{E}_1$ with $\mathbf{E}_2$ in Eq. (7)]. Hence the electron acts as a conversion medium that transfers energy between mode 2 and 1.

For a system with multiple bands, $Q_\alpha[\mathbf{k}] = \sum_i W(\mathbf{k} - \mathbf{k}_i) q_i s_{i,\alpha}$, where the index $s_{i,\alpha}$ encodes how Weyl point i connects the bands of the system (see Sec. I). We hence arrive at

$$\bar{P}_\alpha(\mathbf{k}) = h f_1 f_2 \sum_i W(\mathbf{k} - \mathbf{k}_i) q_i s_{i,\alpha}. \tag{16}$$

This constitutes one of our main results.

Eq. (16) shows that each electron in the Weyl semimetal transfers energy from mode 2 to mode 1 at a rate which is *quantized*, as an integer multiple of $h f_1 f_2$. The value of the integer depends on the location of the electron in the Brillouin zone, $\mathbf{k}$. Specifically, the conversion rate $\bar{P}_\alpha(\mathbf{k})$ is nonzero for electrons whose wavevectors $\mathbf{k}$ are located within the surface $\mathcal{B}_0$ relative to a Weyl point. Thus, a nonzero conversion power can be realized for electrons near Weyl points.

The energy conversion predicted in Eq. (16) can be seen as a realization of the topological frequency conversion that was discovered in Ref. [31]. Ref. [31] showed that a 2-level system (such as a spin-1/2) initialized in its lower band and adiabatically driven by two modes with frequencies f_1 and f_2 can transfer energy between the modes at an average rate quantized as $h f_1 f_2 z$, where z is an integer. Ref. [31] explained this conversion as an anomalous velocity along the synthetic dimensions that correspond to the photon numbers of the two modes. To understand the relationship between our result and Ref. [31], note that for fixed $\mathbf{k}$, $H(\mathbf{k}, t)$ is a Hamiltonian of a 2-level system of the exact same form as considered Ref. [31], with the pseudospin of the electron playing the role of the physical spin in Ref. [31]. Indeed, the arguments of Ref. [31] show that for the two-level system described by $H(\mathbf{k}, t)$, $z = W(\mathbf{k})$. In this way, each electron in a Weyl semimetal can be seen as a topological frequency converter from Ref. [31], with the quantized rate of conversion controlled by its location in the Brillouin zone.

A. Commensurate frequencies

The discussion above for simplicity assumed the frequencies f_1 and f_2 commensurate. Here we consider the case where the frequencies of the modes are commensurate such that $f_1/f_2 = p/q$ for some integers p and q. In this case, $\mathbf{E}(t)$ and $\mathbf{A}(t)$ thus are time-periodic with the extended period $T_{\text{ext}} = pT_1 = qT_2$. This time-periodicity significantly affects the electron's trajectory in the BZ (relative to its equilibrium wavevector), $e\mathbf{A}(t)/\hbar$. For incommensurate frequencies, the trajectory fills a closed surface, namely $\mathcal{B}_0$, as illustrated in Fig. 2(b). In contrast, commensurate frequencies causes the trajectory to form a closed *curve*, $\mathcal{C}_0$, as in Fig. 2(d). The curve $\mathcal{C}_0$ is still located on the surface $\mathcal{B}_0$.

For commensurate frequencies, the driving experienced by the electron depends on the initial phase difference between the modes, $\Delta\phi$; here nonzero $\Delta\phi$ corresponds to a shift of the phase of mode 2 such that $\mathbf{E}(t) = \mathbf{E}_1(t) + \mathbf{E}_2(t + \Delta\phi/\omega_2)$, resulting in $\mathbf{E}(t) = \boldsymbol{\epsilon}(\omega_1 t, \omega_2 t + \Delta\phi)$ and $\mathbf{A}(t) = \boldsymbol{\alpha}(\omega_1 t, \omega_2 t + \Delta\phi)$. For incommensurate frequencies, different values of $\Delta\phi$ are equivalent to shifts in the time origin and hence do not affect the long-term dynamics of the electron. In contrast, for commensurate frequencies, each distinct value of $\Delta\phi$ results in a different closed trajectory of $\mathbf{A}(t)$, $\mathcal{C}_0$. The surface $\mathcal{B}_0$ is recovered by combining the curves $\mathcal{C}_0$ for all possible values of $\Delta\phi$.

For commensurate frequencies, the quantization of $\bar{P}$ breaks down. The breakdown of quantization arises because the trajectory of the modes' phases $(\phi_1(t), \phi_2(t)) = (\omega_1 t, \omega_2 t + \Delta\phi)$ does not cover the whole 2d phase Brillouin zone over time, $\phi_1, \phi_2 = [0, 2\pi)$, thus invalidating the step leading to Eq. (10). However, quantization is recovered when averaging $\bar{P}$ over all possible values of $\Delta\phi$: for commensurate frequencies, Eq. (10) remains valid for the *average* value of $\bar{P}$ with respect to $\Delta\phi$. This phase-averaging can be justified in realistic situations where phase difference of the modes is effectively random.

III. FREQUENCY CONVERSION IN MANY-BODY SYSTEMS

Our next goal is to show how topological frequency conversion emerges in a realistic Weyl semimetal where electrons are affected by interactions, impurities and phonons. We focus on the rate of energy transfer to mode 1 per unit volume for a Weyl semimetal driven by two modes, $\eta(t)$. If $\eta(t)$ is positive, there is a net flow of energy into mode 1, implying amplification of this mode. This energy must originate from mode 2. The conversion rate $\eta(t)$ can be computed from the current density, $\mathbf{j}(t)$, using Ohms law:

$$\eta(t) = -\mathbf{E}_1(t) \cdot \mathbf{j}(t). \tag{17}$$

To obtain the current density $\mathbf{j}(t)$ we characterize the many-body state of the Weyl semimetal in terms of the

momentum resolved density matrix,

$$\hat{\rho}(\mathbf{k},t) \equiv \mathrm{Tr}_{\mathbf{k}'\neq\mathbf{k}}[\hat{\rho}_{\mathrm{F}}(t)], \tag{18}$$

where $\hat{\rho}_{\mathrm{F}}(t)$ denotes the full density matrix of the Weyl semimetal at time t, which is subject to interactions, impurities, and phonons, while $\mathrm{Tr}_{\mathbf{k}'\neq\mathbf{k}}[\cdot]$ denotes the trace over all possible occupations of electronic states with crystal momentum other than $\mathbf{k}$. $\hat{\rho}(\mathbf{k},t)$ is a matrix in the 2^d dimensional Fock space associated with the d orbitals (or bands) accessible by the electrons at wavevector $\mathbf{k}$ [60] Below, the "hat" accent $\hat{\cdot}$ indicates operators that act on many-body orbital Fock states. Operators without the accent, such as the Bloch Hamiltonian from Secs. I-II, $H(\mathbf{k},t)$, are single-particle operators. $\hat{\rho}(\mathbf{k},t)$ encodes the band occupancies alongside with inter-band coherences and all multi-particle correlations of electrons with the same wavevector $\mathbf{k}$. The inter-band coherences are crucial for capturing topological energy conversion, since they give rise to the anomalous velocity in our formalism.

$\hat{\rho}(\mathbf{k},t)$ determines the current density in the system, $\mathbf{j}(t)$, through

$$\mathbf{j}(t) = -\frac{e}{\hbar}\int \frac{\mathrm{d}^3\mathbf{k}}{(2\pi)^3}\mathrm{Tr}[\hat{\rho}(\mathbf{k},t)\nabla_{\mathbf{k}}\hat{H}(\mathbf{k},t)], \tag{19}$$

where momentum integrals are taken over the full Brillouin zone, and $\hat{H}(\mathbf{k},t)$ denotes the second-quantized Bloch Hamiltonian of the system:

$$\hat{H}(\mathbf{k},t) = \sum_{ij} H_{ij}(\mathbf{k},t)\hat{c}_i^\dagger \hat{c}_j, . \tag{20}$$

Here $H_{ij}(\mathbf{k},t) \equiv \langle i|H(\mathbf{k},t)|j\rangle$, and $|i\rangle$ denotes the ith orbital state in the standard Bloch space.

In the presence of driving $\hat{\rho}(\mathbf{k},t)$ approaches to a time-dependent steady state. We obtain this steady state by solving a master equation for $\hat{\rho}(\mathbf{k},t)$, in which the effects of interactions, impurities and disorder are included as a dissipative term. The master equation and steady-state solution are summarized in Sec. III A below. The calculation of the steady-state is straightforward, but involved, and is detailed in Appendix B. A key feature of the steady-state solution is that the current response can be split into an energy-conserving "adiabatic component", $\mathbf{j}_0(t)$, and a dissipative correction due to non-adiabaticity and scattering, $\delta\mathbf{j}(t)$:

$$\mathbf{j}(t) = \mathbf{j}_0(t) + \delta\mathbf{j}(t). \tag{21}$$

This decomposition allows us to identify an energy-conserving and dissipative component of $\eta(t)$:

$$\eta_0(t) = -\mathbf{E}_1(t)\cdot\mathbf{j}_0(t), \quad \eta_{\mathrm{dis}}(t) \equiv -\mathbf{E}_1(t)\cdot\delta\mathbf{j}(t). \tag{22}$$

The component $\mathbf{j}_0(t)$ is responsible for topological frequency conversion, and we find that this term dominates in the limit of adiabatic driving and slow relaxation. As a central result, we find that

$$\mathbf{j}_0(t) \equiv -e\int \frac{\mathrm{d}^3\mathbf{k}}{(2\pi)^3}\sum_\alpha \bar{\rho}_\alpha(\mathbf{k})\dot{\mathbf{r}}_\alpha(\mathbf{k},t) \tag{23}$$

with $\dot{\mathbf{r}}_\alpha(\mathbf{k},t) = \frac{1}{\hbar}\nabla_{\mathbf{k}}\varepsilon_\alpha(\mathbf{k}+e\mathbf{A}(t)) - \frac{e}{\hbar}\mathbf{E}(t)\times\mathbf{\Omega}_\alpha(\mathbf{k}+e\mathbf{A}(t)/\hbar)$ denoting the wavepacket velocity in band α; $\bar{\rho}_\alpha(\mathbf{k})$ is the time-averaged occupation in the αth band of the instantaneous Bloch Hamiltonian, $H(\mathbf{k},t)$.

In what follows, we first discuss the steady state solution of the density matrix (Sec. III A). We then compute the time-averaged energy pumping resulting from the non-dissipative component of the current response, η_0. We finally consider the dissipative component of η, η_{dis} in Sec. III C. It is crucial to estimate η_{dis}, since amplification is only achieved when η_0 exceeds η_{dis}.

A. Steady state solution

We now discuss how we obtain the steady-state of $\hat{\rho}(\mathbf{k},t)$. Details of this discussion are provided in Appendix B.

For a clean and non-interacting system, $\hat{\rho}(\mathbf{k},t)$ evolves according to the von Neumann equation, $\partial_t\hat{\rho}(\mathbf{k},t) = -(i/\hbar)[\hat{H}(\mathbf{k},t),\hat{\rho}(\mathbf{k},t)]$. Interactions, phonons, and impurities cause a dissipative correction to this equation. For sufficiently weak dissipation, this correction can be derived approximately from first principles and takes the form of a trace- and positivity-preserving linear operator acting on $\hat{\rho}(\mathbf{k},t)$, $\mathcal{D}(\mathbf{k},t)$ [61]. Thus, $\hat{\rho}(\mathbf{k},t)$ is governed by the following Lindblad-type quantum master equation

$$\partial_t\hat{\rho}(\mathbf{k},t) \approx \frac{-i}{\hbar}[\hat{H}(\mathbf{k},t),\hat{\rho}(\mathbf{k},t)] + \mathcal{D}(\mathbf{k},t)\circ\hat{\rho}(\mathbf{k},t). \tag{24}$$

In Appendix. B, we obtain a solution to Eq. (24). The solution $\hat{\rho}(\mathbf{k},t)$ is accurate as long as the driving is adiabatic with respect to the energy gap of $H(\mathbf{k},t)$, $\delta\varepsilon$, and much faster than the the magnitude of the dissipator $\mathcal{D}$ [62]:

$$\|\mathcal{D}(\mathbf{k},t)\| \ll \omega_1,\, \omega_2 \ll \delta\varepsilon. \tag{25}$$

We term this limit, as the *coherent adiabatic regime*.

When the above conditions are satisfied, we find the steady state value of $\hat{\rho}(\mathbf{k},t)$ is diagonal in the eigenbasis of the Hamiltonian, $\hat{H}(\mathbf{k},t)$, up to minor nonadiabatic corrections. The corresponding eigenvalues (which determine the the occupations of the instantaneous bands of $\hat{H}(\mathbf{k},t)$) are nearly stationary, except for minor fluctuations of order $\|\mathcal{D}\|/\mathcal{O}(\omega_1,\omega_2)$. These fluctuations, along with the subleading (second-order) nonadiabatic corrections to $\hat{\rho}(\mathbf{k},t)$ give rise to the dissipative current $\delta j(t)$. The term $\mathbf{j}_0(t)$ results from just keeping the (dominating) time-independent component of the eigenvalues of $\hat{\rho}(\mathbf{k},t)$ and including leading-order nonadiabatic correction to its eigenbasis. Here the leading-order non-adiabatic correction to the eigenbasis is responsible for the anomalous velocity which enters in $\mathbf{j}_0(t)$.

Our solution to Eq. (24) applies to any dissipator $\mathcal{D}$, and this dissipator can be derived from first principles [61]. However, for illustrative purposes, we now demonstrate our solution for the concrete example where

$\mathcal{D}$ takes a particular phenomenological form: the "Boltzmann" form. In this approximation, the dissipator uniformly relaxes electrons towards their instantaneous equilibrium state at some given ambient temperature $1/\beta$ and chemical potential μ, and with some rate $1/\tau$:

$$\mathcal{D}_{\mathrm{B}}(\mathbf{k},t)\circ\hat{\rho}=-\frac{1}{\tau}[\hat{\rho}-\hat{\rho}_{\mathrm{eq}}(\mathbf{k},t)]. \tag{26}$$

Here $\hat{\rho}_{\mathrm{eq}}(\mathbf{k},t)$ is the instantaneous equilibrium state described above, and is given by $e^{-\beta[\hat{H}(\mathbf{k},t)-\mu\hat{n}]}/\mathrm{Tr}(e^{-\beta[\hat{H}(\mathbf{k},t)-\mu\hat{n}]})$, where $\hat{n}=\sum_i\hat{c}_i^\dagger\hat{c}_i$. We also use this dissipator in our numerical simulations (see Sec. IV).

The Boltzmann-form dissipator [Eq. (26)] leads to the following steady state density matrix:

$$\bar{\rho}_\alpha(\mathbf{k})\approx\lim_{t\to\infty}\frac{1}{t}\int_0^t \mathrm{d}s\, f_\beta[\varepsilon_\alpha(\mathbf{k},t)-\mu]. \tag{27}$$

where $f_\beta(E)$ denotes the Fermi-Dirac distribution at temperature $1/\beta$. This result (see also Appendix B) indicates a steady state occupation which is the average band-population on the trajectory $\mathbf{k}+e\mathbf{A}(t)/\hbar$, as if the equilibrium distribution is "smeared" over a characteristic wavevector scale $eA/\hbar$, where A is the drive vector potential magnitude. This smearing is confirmed in our numerical simulations (see Sec. IV and Fig. 4 in particular).

B. Non-dissipative frequency conversion

We first compute the average rate of energy transfer in the limit of adiabatic driving and zero dissipation. I.e., we compute the the time-average of the component $\eta_0(t)$, $\bar{\eta}_0$. We find that $\eta_0(t)$ can have nonzero time-average because of the mechanism of topological frequency conversion that we discovered in the last section.

To compute $\bar{\eta}_0$ we first note η_0 can be written

$$\eta_0(t)=\sum_\alpha\int\frac{\mathrm{d}^3\mathbf{k}}{(2\pi)^3}\bar{\rho}_\alpha(\mathbf{k})P_\alpha(\mathbf{k},t) \tag{28}$$

where $P_\alpha(\mathbf{k},t)\equiv e\mathbf{E}(t)\cdot\dot{\mathbf{r}}_\alpha(\mathbf{k},t)$ [see also Eq. (7)]. We find the time-average of the above using the main result from Sec. III B, $\bar{P}_\alpha(\mathbf{k})=-hf_1f_2\sum_i W(\mathbf{k}-\mathbf{k}_i)q_is_{i,\alpha}$ [Eq. (16)]. Here q_i, $s_{i,\alpha}$, and $\mathbf{k}_i$ denote the charge, band connectivity, and wave vector of Weyl point i in the system, respectively, while $W(\mathbf{k})$ measures the net winding of the surface $\mathcal{B}_0$ around wavevector $\mathbf{k}$ (see Sec. III C for further details). with this, Eq. (28) becomes:

$$\bar{\eta}_0=-hf_1f_2\sum_{\alpha,i}\int\frac{\mathrm{d}^3\mathbf{k}}{(2\pi)^3}q_is_{i,\alpha}\bar{\rho}_\alpha(\mathbf{k})W(\mathbf{k}-\mathbf{k}_i). \tag{29}$$

Thus, each Weyl point is surrounded by a region of reciprocal space (namely the region where $W(\mathbf{k}-\mathbf{k}_i)\neq 0$), in which electrons act as topological frequency converters. In this region, each transfers energy to mode 1 at the quantized rate $\pm hf_1f_2$. This is a many-electron generalization of Eq. (16) and constitutes another main results of this paper.

In the following we thus refer to $\bar{\eta}_0$ as the topological frequency conversion rate of the system, to distinguish it from the dissipation rate, which is given by the time-average of $\eta_{\mathrm{dis}}(t)$.

The rate of topological energy conversion can potentially be quite large for realistic parameters. $W(\mathbf{k})$ is positive within volume of order $\sim 4(eA/\hbar)^3$ in reciprocal space, corresponding to an electronic density of $4(eA/2\pi\hbar)^3$ for each Weyl point. Since each electron contributes hf_1f_2 to $\bar{\eta}_0$, the "gross" rate of topological frequency conversion from a Weyl point (i.e., not taking into account cancellation between electrons that transfer energy at opposite rates) is of order

$$\eta_{\mathrm{gross}}\sim\frac{e^3E^3}{4\pi^4\Omega\hbar^2}. \tag{30}$$

Here, E denotes the characteristic magnitude of $\mathbf{E}(t)$, Ω denotes the characteristic scale of ω_1 and ω_2, and we used $A\sim E/\Omega$. For $\Omega\sim 2\pi\,\mathrm{THz}$ and $E\sim 1.5\mathrm{MV}\cdot\mathrm{m}$ (corresponding to intensities of $6\mathrm{kW/mm}^2$, which we expect can be reached using pulsed lasers [63]) the above estimate yields $\eta_{\mathrm{gross}}\sim 500\,\mathrm{kW/mm}^3$.

The actual, *net*, topological conversion power, $\bar{\eta}_0$ is significantly smaller than the gross rate we estimated above, due to cancellation between electrons that convert energy at rates hf_1f_2 and $-hf_1f_2$. Specifically, when modes 1 and 2 only contain a single harmonic each, the driving induced vector potential satisfies $\mathbf{A}_i(t)=-\mathbf{A}_i(t+T_i/2)$, implying $W(\mathbf{k})=-W(-\mathbf{k})$ [64] [this symmetry is clearly evident in Fig. 2(c)]. Hence the regions of reciprocal space characterized by conversion rates hf_1f_2 and $-hf_1f_2$ have equal net volumes. In realistic situations, both volumes will be occupied by electrons, implying $\bar{\eta}_0\ll\eta_{\mathrm{gross}}$. However, because η_{gross} can be quite large, even a small imbalance in the filling of the two regions can lead to significant net frequency conversion.

To achieve a nonzero $\bar{\eta}_0$, the steady-state occupation of the bands, $\bar{\rho}_\alpha(\mathbf{k})$, must be anisotropic around the Weyl point to counteract the antisymmetry $W(\mathbf{k})=-W(-\mathbf{k})$. Such an anisotropy is generally achieved when the "Weyl cone tilt", $\mathbf{V}$, is nonzero, since we expect the steady-state inherits the same symmetry properties as the equilibrium state [see Eq. (1)]. Additionally, the Weyl point must be within a distance of order $\sim eA/\hbar$ from the Fermi surface to ensure that $\bar{\rho}_\alpha(\mathbf{k})$ does not take constant value (1 or 0) within $\mathcal{B}_0$. Indeed, our numerical simulations demonstrate that nonzero $\bar{\eta}_0$ can arise when $\mathbf{V}\neq 0$ and the Fermi surface lies close to the Weyl point.

Topological frequency conversion is a highly nonlinear effect: it emerges only when the driving vector potential exceeds a certain threshold, namely when the surface $\mathcal{B}_0$ becomes large enough to enclose $\mathbf{k}$-points where the gap of $H(\mathbf{k})$ is larger than Ω (see Sec. III C 2 for further discussion) and also large enough so that the Fermi surface

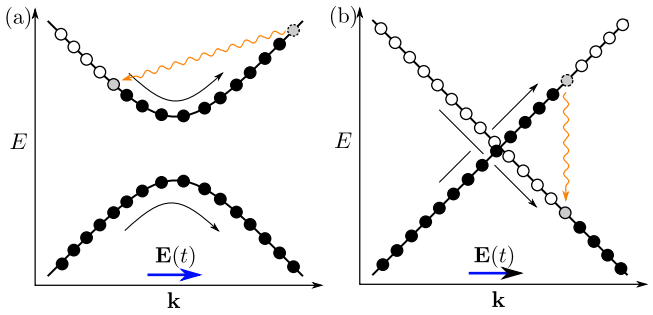

FIG. 3. Schematic illustration of the two distinct dissipation mechanisms in a driven Weyl semimetal. (a) Momentum relaxation: as electrons are adiabatically translated in the Brillouin zone by the driving-induced electric field (black arrows), electrons shifted to higher energies (black dots) can relax by decaying to vacant states that have become available at lower energies within the same band (white dots), causing net dissipation of energy. This mechanism can occur for all wavevectors near the Fermi surface, where driving increases the energy of electrons beyond the energies of vacant states elsewhere in the same band. (b): Nonadiabatic heating. Electrons that are taken through or near a Weyl node by the driving-induced electric field can undergo complete or partial Landau-Zener tunneling from the valence to the conduction band. This results in dissipation when the excited electrons in the conduction band relax back into vacant states in the valence band.

is within a distance $\sim A$ from the Weyl point). Hence topological frequency conversion does not have a simple power-law dependence on A in the limit of small A, and is therefore beyond by standard nonlinear response theory.

C. Dissipative energy loss

For topological frequency conversion to cause a net amplification of mode 1, $\bar{\eta}_0$ must exceed the rate of energy loss due to dissipation, $\eta_{\rm dis}$. It is therefore crucial to estimate this dissipation rate. This is the goal of this subsection.

Our solution of the master equation in Appendix B shows that the dissipative current response, $\delta\mathbf{j}(t)$ [see Eq. (21)], contains two components:

$$\delta\mathbf{j}(t) = \delta\mathbf{j}_{\rm mr}(t) + \delta\mathbf{j}_{\rm na}(t), \tag{31}$$

which we interpret as arising from momentum-relaxation ($\delta\mathbf{j}_{\rm mr}$) and nonadiabaticity-induced particle-hole pair creation ($\delta\mathbf{j}_{\rm na}$); see discussion below. Consequently, $\eta_{\rm dis}(t)$ can also be separated into these two components:

$$\eta_{\rm dis}(t) = \eta_{\rm mr}(t) + \eta_{\rm na}(t). \tag{32}$$

where $\eta_{\rm mr}(t) \equiv \mathbf{E}_1(t)\cdot\mathbf{j}_{\rm mr}(t)$, and $\eta_{\rm na}$ is defined likewise.

While $\eta_{\rm mr}$ and $\eta_{\rm na}$ are given in Appendix B, here we discuss their origin and estimate their magnitudes based on a phenomenological discussion.

Energy loss due to momentum relaxation, $\eta_{\rm mr}$, arises when perturbed electrons in the close vicinity the Fermi surface relax due to their displacement from instantaneous equilibrium, as schematically indicated in Fig. 3(a). In contrast, $\eta_{\rm na}(t)$ arises from the particle-hole pair creation that results because the driving-induced electric field inevitably overpowers the gap sufficiently close to Weyl points. Equivalently, $\eta_{\rm na}$ arises because effective gap closing of $\hat{H}(\mathbf{k},t)$ near a Weyl point gives rise to Landau-Zener tunneling from the conduction to the valence band upon driving. These excited electrons dissipate energy as they relax back to the conduction band, as schematically illustrated in Fig. 3(b).

Below we estimate $\eta_{\rm mr}$ and $\eta_{\rm na}$ based on phenomenological arguments. For simplicity, we consider system with two bands and an isolated Weyl point at $\mathbf{k}=0$ (which is easily generalized to multiple Weyl points). Moreover, we do not distinguish between the characteristic relaxation rates associated with momentum relaxation and particle-hole pair creation (which may be different in real materials), but use

$$\Gamma \sim \|\mathcal{D}(\mathbf{k},t)\| \tag{33}$$

as an estimate for both characteristic relaxation rates.

1. *Momentum relaxation*

We first estimate the rate of energy loss arising from momentum relaxation, $\eta_{\rm mr}(t)$.

Effects of momentum relaxation can only emerge within a distance $\sim eA/\hbar$ from the Fermi surface, where electronic occupation fluctuates. Therefore, only a density of $eS_{\rm F}A/(2\pi)^3\hbar$ contributes to $\delta\mathbf{j}_{\rm mr}(t)$, where S_F is the area of the Fermi surface. Electrons near the Fermi surface on average gain an energy of order $eAv_{\rm F}/2\hbar$ due to the driving (with $v_{\rm F}$ the characteristic Fermi velocity). Assuming their relaxation rate is of order Γ, the average rate of energy loss in the system due to momentum relaxation thus is given by $\frac{\Gamma e^2A^2S_{\rm F}v_{\rm F}}{16\pi^3\hbar}$. We estimate that half of this comes from mode 1. This estimate agrees well with our predictions based on the definition of $\delta\mathbf{j}_{\rm mr}(t)$ in Appendix B. Using that $A\sim E/\Omega$, along with $E^2\sim I/c\epsilon_0$, where I denotes the radiation intensity, and c the speed of light, we thus obtain

$$\eta_{\rm mr} \sim \frac{\Gamma e^2 I S_{\rm F} v_{\rm F}}{16\pi^3 c\epsilon_0\hbar\Omega^2}. \tag{34}$$

It is interesting to note that $\eta_{\rm mr}$ is proportional to the size of the Fermi surface, $S_{\rm F}$. Therefore type-I Weyl points are more suitable for frequency conversion than type-II Weyl semimetals, since the surrounding Fermi surface forms a compact ellipsoid for the former case, in contrast to an extended hyperboloid in the latter.

As an example, we estimate $\eta_{\rm mr}$ for the same parameters we used to estimate $\eta_{\rm gross}$ in Sec. III B i.e., $I = 6\,\mathrm{kW/mm^2}$, $v_{\rm F}\sim 5\cdot 10^5\mathrm{m/s}$, $\Omega = 2\pi\,\mathrm{THz}$.

For an ellipsoid Fermi surface with principal semi axes $(1.5, 1.5, 2.4)eA/\hbar$ (yielding $S_{\rm F} \approx 0.06\text{Å}^{-2}$), our estimate then results in $\eta_{\rm mr} \sim 5 \cdot 10^{-5}\text{J/mm}^3\tau$, where $\tau = 1/\Gamma$. Note that our estimated value of $\eta_{\rm mr}$ is proportional to the Fermi surface area and thus can be easily adjusted to other values of this quantity. Recalling that $\eta_{\rm gross} \sim 500\,\text{kW/mm}^3$ for the same parameters, we expect net frequency conversion to only exceed momentum relaxation when $\tau \gg 100\,\text{ps}$. This expectation is confirmed in our numerical simulations [see Fig. 1(b)].

2. Non-adiabatic heating

Non-adiabatic heating arises from electrons at $\mathbf{k}$-points where the time-dependence of $H(\mathbf{k}, t) = H(\mathbf{k} + e\mathbf{A}(t)/\hbar)$ overwhelms the band gap. In Weyl semimetals, such $\mathbf{k}$-points inevitably exist (even for arbitrarily slow driving), because the band gap of $H(\mathbf{k})$ closes at Weyl points. For each such $\mathbf{k}$-point, the band gap of $H(\mathbf{k}, t)$ effectively closes at certain times t, namely when $\mathbf{k} + e\mathbf{A}(t)/\hbar$ is sufficiently close to the Weyl point at $\mathbf{k} = 0$ (see below for more detailed conditions). At each such gap-closing event, electrons at wavevector $\mathbf{k}$ will undergo partial or complete Landau-Zener transition from the conduction to the valence band. This mechanism effectively heats the electrons and eventually results in dissipation once the excited electrons relax. The dissipation induced by the mechanism above is captured by $\eta_{\rm na}(t)$.

To estimate $\eta_{\rm na}$ we first identify the set of $\mathbf{k}$-points for which the time-dependence of $H(\mathbf{k}, t)$ is non-adiabatic; we term this region of reciprocal space as the "non-adiabatic" region and denote it by $\mathcal{V}_{\rm na}$. The Landau-Zener formula [65, 66] states that time-dependence of $H(\mathbf{k}, t)$ is non-adiabatic if, for some t,

$$\hbar\|\partial_t H(\mathbf{k} + e\mathbf{A}(t))\| \gtrsim \delta\varepsilon^2(\mathbf{k} + e\mathbf{A}(t))/\hbar, \tag{35}$$

where $\delta\varepsilon(\mathbf{k}) \equiv \varepsilon_2(\mathbf{k}) - \varepsilon_1(\mathbf{k})$, and $\varepsilon_\alpha(\mathbf{k})$ denotes the αth energy band of $H(\mathbf{k})$. Using the linearized form of $H(\mathbf{k})$ in Eq. (1), a straightforward derivation (see Appendix C) shows that this condition is satisfied at $\mathbf{k}$-points for which $\min_t |\mathbf{k} + e\mathbf{A}(t)/\hbar| \gtrsim d_0$ where

$$d_0 \equiv \sqrt{\frac{eE\|R\|}{\hbar v_0^2}}, \tag{36}$$

while $\|R\|$ and v_0 denotes the largest and smallest eigenvalue of the velocity matrix R, respectively [see Eq. (1)] [67]. For incommensurate frequencies, $\mathcal{V}_{\rm na}$ thus consists of all $\mathbf{k}$-points within a distance d_0 from the topological phase boundary $\mathcal{B}_0$ by our estimate. For commensurate frequencies $\mathcal{V}_{\rm na}$ consists all $\mathbf{k}$-points within a distance d_0 from $\mathcal{C}_0$, which forms a closed curve on $\mathcal{B}_0$, as in Fig. 2(d).

Electrons with wave vectors $\mathbf{k}$ within $\mathcal{V}_{\rm na}$ encounter a vanishing gap of $\hat{H}(\mathbf{k}, t)$ at times t where $|\mathbf{k} + e\mathbf{A}(t)/\hbar| \lesssim d_0$. These electrons then undergo Landau-Zener tunneling, which effectively heats them to a high-temperature state, as explained in the beginning of this subsection. These high-temperature electrons then relax back to equilibrium after a characteristic time $1/\Gamma$. $\eta_{\rm na}(t)$ is then the rate of energy loss, or heating, (per unit volume) arising from this relaxation. We estimate

$$\eta_{\rm na} \sim \Delta\varepsilon_{\rm na} n_{\rm na}\Gamma/2, \tag{37}$$

where $n_{\rm na}$ is the concentration of excited electrons within $\mathcal{V}_{\rm na}$, and $\Delta\varepsilon_{\rm na}$ denotes the characteristic average value of $\delta\varepsilon(\mathbf{k}+e\mathbf{A}(t))$ for $\mathbf{k}$ within $\mathcal{V}_{\rm na}$. Here the factor of 2 comes because we estimate that the other half of the dissipated energy comes from mode 2.

We obtain $\Delta\varepsilon_{\rm na}$ using that $\mathcal{V}_{\rm na}$ is located a distance $\sim eA/\hbar$ from the Weyl node, such that $\Delta\varepsilon_{\rm na} \sim eA\|R\|$, and $\|R\|$ is the largest velocity implied by the velocity tensor R. Using $A \sim E/\Omega$, we obtain

$$\Delta\varepsilon_{\rm na} \lesssim eE\|R\|/\Omega. \tag{38}$$

To estimate $n_{\rm na}$, it is crucial to know the characteristic time interval between successive gap-closing events experienced by electrons with a given wavevector within $\mathcal{V}_{\rm na}$, Δt. To build intuition, let us first consider what happens when $\Delta t \gg 1/\Gamma$, i.e., when electrons have time to fully relax between successive gap-closing events [68]. Electrons at wavevector $\mathbf{k}$ are taken to a high-temperature state whenever $\mathbf{k}$ comes within a sphere of radius $\sim d_0$ from $e\mathbf{A}(t)/\hbar$. Electrons are in equilibrium as they "enter" the sphere (due to our assumption $\Delta t \gg 1/\Gamma$), and we estimate that half of them are excited to the conduction band as they "leave" the sphere. The concentration of electrons per unit time that are heated by this process is hence given by the cross-section of this sphere times $\frac{0.5}{(2\pi)^3} e|\partial_t \mathbf{A}|/\hbar$. Therefore, we expect the concentration of electrons heated per unit time to be given by $ed_0^2|\partial_t \mathbf{A}(t)|/16\pi^2\hbar$. Assuming the electrons relax with characteristic rate Γ, we estimate $n_{\rm na}$ as the fixed point of $\partial_t n_{\rm na} = e\pi d_0^2|\partial_t \mathbf{A}(t)|/16\pi^2\hbar - \Gamma n_{\rm na}$. Using $\partial_t \mathbf{A} = E$, we thus find $n_{\rm na} \sim ed_0^2 E/16\pi^2\hbar\Gamma$.

Next, we consider the case where $\Delta t \lesssim 1/\Gamma$. In this case, a significant fraction of electrons are already in a high-temperature state when they experience a gap-closing event (i.e., when they "enter" the sphere with radius d_0 centered at $e\mathbf{A}(t)/\hbar$). Assuming that the gap-closing event effectively randomizes the state of the electrons (i.e., the electrons are in a infinite-temperature state right after "leaving" the sphere, regardless of their initial state), a subsequent gap-closing event only re-heats a reduced number of electrons to a high-temperature state. We estimate the fraction of pre-excited electrons to be of order $0.5\,e^{-\Gamma\Delta t}$ right before the gap closing and 0.5 right after; thus the heating rate is reduced by a factor $\mathcal{O}(1 - e^{-\Gamma\Delta t})$, resulting in

$$n_{\rm na} \sim \frac{ed_0^2 E}{16\pi^2\hbar\Gamma}(1 - e^{-\Gamma\Delta t}). \tag{39}$$

Combining this result with Eqs. (36)-(38), we obtain

$$\eta_{\rm na} \sim \frac{e^3 E^3\|R\|^2}{32\pi^2\hbar^2\Omega v_0^2}(1 - e^{-\Gamma\Delta t}). \tag{40}$$

Below we estimate Δt (i.e., the characteristic time between gap closing events) for the two cases incommensurate and commensurate frequencies; as we find these two situations lead to significantly different Δt, and hence also different values of $\eta_{\rm na}$.

Evidently, the bound above is controlled by the ratio between the largest and smallest eigenvalues of the matrix R, $\|R\|/v_0$. As we argued in Sec. I, this number quantifies the anisotropy of the band gap around the Weyl point.

Note that the first factor in Eq. (40) is larger than the *gross* rate of topological frequency conversion in Eq. (30) (this follows from $\|R\|/v_0 \geq 1$, and $\pi^2 > 8$). Thus, Δt, needs to be much shorter than Γ^{-1} for nonadiabatic heating not to overwhelm the net rate of topological frequency conversion. In particular, since Δt is at least $2\pi/\Omega$, we expect $\Gamma \ll \Omega$ to be a necessary condition for topological frequency conversion.

To illustrate the above result, we estimate $\eta_{\rm na}$ for the same parameters as gave us the estimates $\eta_{\rm gross} = 500\,{\rm kW/mm^3}$ and $\eta_{\rm mr} \sim 100\,{\rm kW/mm^3}$, namely, $I = 6\,{\rm kW/mm^2}$, $\Omega = 2\pi\,{\rm THz}$, $\|R\| \sim v_0 \sim 5\cdot 10^5 {\rm m/s}$ [see text below Eqs. (30) and Eq. (34)]. With these parameters Eq. (40) yields $\eta_{\rm na} \sim 650{\rm kW/mm^3}(1-e^{-\Gamma\Delta t})$. In the case of fast relaxation Γ, $\eta_{\rm na}$ is clearly the dominant heating mechanism.

3. *Nonadiabatic heating at incommensurate frequencies*

For incommensurate frequencies, we estimate Δt as the time-window over which trajectory of $e\mathbf{A}(t)/\hbar$ has length $|\mathcal{B}_0|/d_0$, where $|\mathcal{B}_0|$ denotes the area of the surface on which $e\mathbf{A}(t)/\hbar$ is confined to at all times, $\mathcal{B}_0 \equiv \{e\boldsymbol{\alpha}(\phi_1,\phi_2),\ 0<\phi_i<2\pi\}$ [see Sec. II and Fig. 2(b)] Since $\partial_t \mathbf{A}(t) = \mathbf{E}(t)$, the trajectory of $e\mathbf{A}(t)/\hbar$ over the time-window Δt has length $eE\Delta t/\hbar$. Estimating $|\mathcal{B}_0| \sim 4\pi^2 e^2 A^2/\hbar^2$ and using $d_0 = \sqrt{eE\|R\|/\hbar v_0^2}$ along with $A \sim E/\Omega$, we hence obtain

$$\Delta t \sim \frac{4\pi^2}{\Omega^2}\sqrt{\frac{eEv_0^2}{\hbar\|R\|}} \quad \text{for irrational } \omega_1/\omega_2 \tag{41}$$

For the parameters we used to estimate $\eta_{\rm na}$ above [$I = 6\,{\rm kW/mm^2}$ (corresponding to $E \sim 1.5\,{\rm MV/m}$), $v_{\rm F} \sim 5\cdot 10^5 {\rm m/s}$, and $\Omega = 2\pi\,{\rm THz}$] this estimate yields $\Delta t \sim 30\,{\rm ps}$. To achieve topological frequency conversion at incommensurate frequencies with these parameters, the characteristic relaxation time $\tau = \Gamma^{-1}$ must be much longer than this timescale. In this limit (i.e., $\tau \gg \Delta t$), we find $\eta_{\rm na} \sim 5\cdot 10^{-8}{\rm kJ/mm^3}\tau$, which is smaller than $\eta_{\rm gross}$ when $\tau \gtrsim 100\,{\rm ps}$.

D. Lissajous Conversion

We now consider the case of commensurate frequencies, which can give a marked reduction of the non-adiabatic losses.

Eq. (40) shows that small time-intervals between subsequent gap-closing events, Δt, leads to suppression of nonadiabatic heating, $\eta_{\rm na}$. An important consequence of this is that $\eta_{\rm na}$ is strongly suppressed for commensurate frequencies, i.e., when

$$f_1/f_2 = q/p \tag{42}$$

for some integers p and q (which we, without loss of generality, take to have no common divisor). In this case, $e\mathbf{A}(t)/\hbar$ forms a 3-dimensional Lissajous figure in reciprocal space, as in Fig. 2(d), and is time-periodic with period $qT_1 = pT_2$. Thus, a given $\mathbf{k}$-point within $\mathcal{V}_{\rm na}$ experiences gap-closing events with periodicity [69]

$$\Delta t = qT_1 = pT_2. \tag{43}$$

As a consequence, $\eta_{\rm na}$ is strongly suppressed for highly rational frequency ratios, i.e., when p and q are small.

The suppression of $\eta_{\rm na}$ means that net amplification from topological frequency conversion is significantly enhanced at highly commensurate frequencies. We term this mechanism of topological frequency conversion at commensurate frequencies *Lissajous conversion*. The dramatic suppression of nonadiabatic heating results in an enhanced net frequency conversion rate in the Lissajous conversion regime, as is evident in our numerical simulations (see Fig. 1(b), and Sec. IV).

As an example, we consider Lissajous conversion at frequencies $\omega_1 = 2\pi\,{\rm THz}$ $\omega_2 = \frac{3}{2}\omega_1$. These parameters result in $\Delta t \sim 3{\rm ps}$. To compare, recall that Δt was estimated to 30 ps in the same frequency range. Using Eq. (37), we estimate the nonadiabatic heating rate to be given by $\eta_{\rm na} \sim 3.5\cdot 10^{-9}{\rm kJ/mm^3}\tau$, which we expect can be smaller than $\eta_{\rm gross}$ when $\tau \gg 10\,{\rm ps}$. In contrast, recall that our estimated nonadiabatic heating rate at incommensurate frequencies in the same frequency range is given by $5\cdot 10^{-8}{\rm kJ/mm^3}\tau$, and thus more than 10 times larger.

In the limit of large p, q, we expect that our estimate for Δt saturates at the expression we obtain for incommensurate frequencies.

IV. NUMERICAL SIMULATIONS

We now support our theoretical predictions by data from numerical simulations.

In our simulations, we consider the dynamics of electrons near a single Weyl node in a Weyl semimetal with 2 bands. The electrons are subject to the linearized Bloch Hamiltonian

$$H(\mathbf{k}) = \hbar v \mathbf{k}\cdot\boldsymbol{\sigma} + \hbar\mathbf{k}\cdot\mathbf{V}. \tag{44}$$

We also introduce two circularly-polarized electromagnetic modes that propagate in the x- and y-directions, respectively. For $i = 1, 2$, mode i has angular frequency

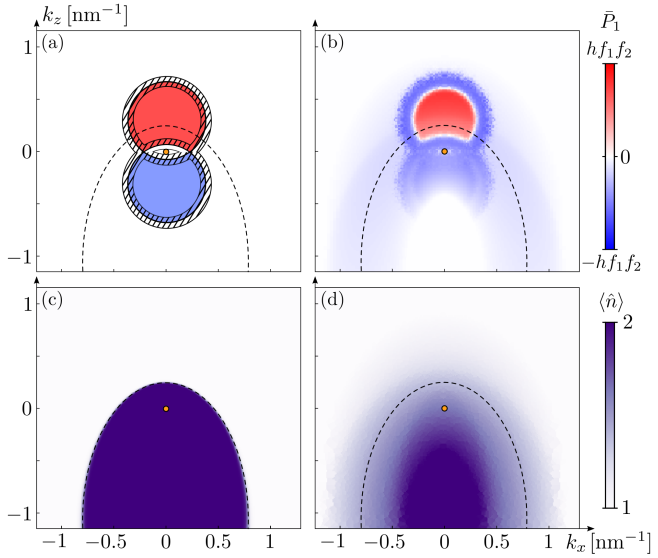

FIG. 4. Energy conversion in the model we study in Sec. IV. (a) Plot of $W(\mathbf{k})$ in the plane $k_y = 0$, with red, blue, and white indicating values -1, 1, and 0, respectively. Black circle indicates $\mathcal{B}_0$ and shaded region schematically indicates the non-adiabatic region $\mathcal{V}_{\rm na}$. Orange circle and dashed line indicate the location of the Weyl point and equilibrium Fermi surface. (b): net rate of energy transfer to mode 1 from electrons with a given wavevector $\mathbf{k}$, $\bar{P}(\mathbf{k})$, as a function of $\mathbf{k}$ in the plane $k_y = 0$, for same parameters as in Fig. 4(a). (c) occupation number in equilibrium of electronic modes with wavevector $\mathbf{k}$, as a function of $\mathbf{k}$ in the plane $k_y = 0$, for the same system as in panels (a-b). (d): net time-averaged occupation number of electronic modes with wavevector $\mathbf{k}$, $\langle\hat{n}(\mathbf{k})\rangle$ as a function of $\mathbf{k}$ in the plane $k_y = 0$ for the system depicted in panel (a-c).

ω_i and electric field amplitude $\mathcal{E}_i$, and thus induces the time-dependent electric field $\mathbf{E}_i(t)$, where

$$\mathbf{E}_1(t) = \mathcal{E}_1(\cos\omega_1 t, 0, \sin\omega_1 t), \tag{45}$$
$$\mathbf{E}_2(t) = \mathcal{E}_2(0, \cos\omega_2 t, \sin\omega_2 t). \tag{46}$$

The irradiated electrons are governed by the time-dependent Bloch Hamiltonian $H(\mathbf{k},t) = H(\mathbf{k}+e\mathbf{A}(t)/\hbar)$, where $\mathbf{A}(t)$ denotes the driving-induced vector potential and is defined through $\partial_t\mathbf{A}(t) = \mathbf{E}_1(t) + \mathbf{E}_2(t)$ (see also Sec. II). As in the previous sections, we work in a gauge where $\mathbf{A}(t)$ has vanishing time-average.

We numerically obtain the evolution of the momentum-resolved density matrix of the system, $\hat{\rho}(\mathbf{k},t)$ (see Sec. III for definition), using the master equation in Eq. (24). We take the dissipator $\mathcal{D}$ to be given by the Boltzmann form [Eq. (26)]: $\mathcal{D}(\mathbf{k},t)\circ\hat{\rho} = -\frac{1}{\tau}[\hat{\rho} - \hat{\rho}_{\rm eq}(\mathbf{k},t)]$. Here $\hat{\rho}_{\rm eq}(\mathbf{k},t)$ denotes the instantaneous equilibrium state of electrons with crystal momentum $\mathbf{k}$ at time t at some given temperature T and chemical potential μ [see text below Eq. (26) for explicit definition]. Since Eq. (24) describes evolution in the 4-dimensional second-quantized Bloch space of the system, its numerical solution is relatively inexpensive.

For each $\mathbf{k}$, we numerically solve Eq. (24) to obtain the steady-state evolution of $\hat{\rho}(\mathbf{k},t)$. From this steady state we extract the quantity

$$\bar{P}(\mathbf{k}) \equiv \lim_{t\to\infty}\frac{1}{t}\int_0^t \mathrm{d}s\,\frac{e}{\hbar}\mathbf{E}_1(s)\cdot\mathrm{Tr}[\nabla\hat{H}(\mathbf{k},s)\hat{\rho}(\mathbf{k},s)]. \tag{47}$$

$\bar{P}(\mathbf{k})$ gives the time-averaged *total* rate of energy transfer to mode 1 from electrons with wavevector $\mathbf{k}$. The total time-averaged rate of energy transferred to mode 1 per unit volume of the whole system, $\bar{\eta}$, is obtained by integrating $P(\mathbf{k})$ over all wavevectors:

$$\bar{\eta} = \int\frac{\mathrm{d}^3\mathbf{k}}{(2\pi)^3}\bar{P}(\mathbf{k}). \tag{48}$$

In our simulation, we evaluate the $\mathbf{k}$-integral above by sampling $\bar{P}(\mathbf{k})$ over a large number of uniformly distributed values of $\mathbf{k}$ [70].

We solve the master equation for $\hat{\rho}(\mathbf{k},t)$ through direct integration, not making use of any of the approximations of Sec. III C. In particular, our simulation does not distinguish between coherent and incoherent dynamics, and our obtained value for $\bar{\eta}$ thus includes both contributions both from topological frequency conversion and dissipation. Hence our simulation can be used to test the conclusions in Sec. III.

We probe different values of f_1 and τ, while keeping all other parameters fixed at values $f_2 = 1.23\,\mathrm{THz}$, $v = 3.87\cdot10^5\,\mathrm{m/s}$, $\mathbf{V} = (0, 0, 3.1\cdot10^5\,\mathrm{m/s})$, $\mu = 115\,\mathrm{meV}$, $T = 20\,\mathrm{K}$, $\mathcal{E}_1 = 0.9\,\mathrm{MV/m}$, and $\mathcal{E}_2 = 1.8\,\mathrm{MV/m}$. Our chosen values of $\mathcal{E}_1$ and $\mathcal{E}_2$ correspond to intensities $2.14\,\mathrm{kW/mm^2}$ and $8.57\,\mathrm{kW/mm^2}$, respectively, which are experimentally accessible with pulsed lasers in some frequency ranges [63]. Our chosen values of v and $\mathbf{V}$ have magnitudes comparable to those in real materials [71, 72]. The values of μ and $\mathbf{V}$ are chosen to maximize the imbalance between the number of electrons acting as frequency converters at rates hf_1f_2 and $-hf_1f_2$, as discussed in Sec. III B (see also Sec. IV B below).

A. Identification of amplification regime

In Sec. III, we showed that the time-averaged rate of energy transfer to mode 1 can be decomposed as $\bar{\eta} = \bar{\eta}_0 + \bar{\eta}_{\rm dis}$. Here $\bar{\eta}_0$ can be positive due to topological frequency conversion, while $\bar{\eta}_{\rm dis}$ is negative and measures the time-averaged rate of energy dissipated from mode 1 due to heating in the system. We expect $|\bar{\eta}_{\rm dis}|$ to decrease with increasing relaxation time τ, while $\bar{\eta}_0$ remains constant. Thus, $\bar{\eta}$ should increase with τ. There should also exist a critical value of τ for which $\bar{\eta} = 0$. When τ is larger than this "amplification threshold", the system will amplify mode 1 ($\bar{\eta} > 0$). We expect the amplification threshold to be significantly lower in the Lissajous conversion regime (i.e., at rational frequency ratios) than for irrational frequency ratios due to the suppression of

nonadiabatic heating in the former case (see Sec. IV C and Sec. IV C below).

To identify the amplification threshold for the system, we computed $\bar{\eta}$ as a function of τ for three representative choices of f_1/f_2; namely, irrational $f_1 = \frac{1}{\varphi} f_2$, rational $f_1 = \frac{2}{3} f_2$, and nearly-rational $f_1 = \frac{2}{3+\epsilon} f_2$, where φ is given by the "golden mean", $\frac{1}{2}(1+\sqrt{5})$, and $\epsilon = \pi/1000$. We keep all other parameters fixed at the values we specified earlier. The two latter values of f_1 are chosen to demonstrate the mechanism of Lissajous conversion: Whereas $f_1 = \frac{2}{3} f_2$ is commensurate with f_2, $f_1 = \frac{2}{3+\epsilon} f_2$ is not, and hence the former value of f_1 is expected to yield more efficient—Lissajous—conversion.

In Fig. 1(b) we plot $\bar{\eta}$ as a function of τ for the three values of f_1 above. As we expect, $\bar{\eta}$ increases as a function of τ for all choices of f_1, and attains positive value for sufficiently large τ. For the irrational frequency ratio $f_1 = f_2/\varphi$, the amplification threshold is reached at $\tau \approx 1000\,\mathrm{ps}$, for $f_1 = 2f_2/3$ at $\tau \approx 300\,\mathrm{ps}$ and for $f_1 = 2f_2/(3+\epsilon)$ above $\tau = 1200\,\mathrm{ps}$.

Note that the weak detuning of f_1 from $2f_2/3$ (green curve) to $2f_2/(3+\epsilon)$ (orange curve) reduces $\bar{\eta}$ by more than $100\,\mathrm{kW/mm^3}$, and pushes the amplification threshold from 300 to 1200 ps. This demonstrates the strong dependence of the net conversion rate on the commensurability of f_1 and f_2 that we discussed in Sec. III D.

B. Origin of energy conversion

Next, we confirm that the amplification of mode 1 (i.e, the positive values of $\bar{\eta} > 0$) we observed is due to topological frequency conversion. To this end, we compute $\bar{P}(\mathbf{k})$ as a function of $\mathbf{k}$ around the Weyl point.

We first review the signatures of topological frequency conversion we expect to see. For $\mathbf{k}$-points where $H(\mathbf{k}, t)$ changes adiabatically in time, electrons should act as topological frequency converters (as in Ref. [31]) that transfer energy to mode 1 at an average rate quantized as $\pm h f_1 f_2 W(\mathbf{k})$, where the $W(\mathbf{k})$ denotes the integer-valued net winding number of the surface $\mathcal{B}_0$ around $\mathbf{k}$ [see Fig. 2(c)]. Here + and − result from electrons in band 1 and 2, respectively. We hence expect

$$\bar{P}(\mathbf{k}) = h f_1 f_2 W(\mathbf{k})[\bar{\rho}_1(\mathbf{k}) - \bar{\rho}_2(\mathbf{k})] + P_{\mathrm{dis}}(\mathbf{k}), \qquad (49)$$

where $\bar{\rho}_\alpha(\mathbf{k})$ denotes the time-averaged occupancy of band α, and $P_{\mathrm{dis}}(\mathbf{k})$ denotes the rate of energy loss from mode 1 due to dissipation. We expect the latter is always negative, but only significant around the Fermi surface (due to momentum relaxation), and within the nonadiabatic region (due to nonadiabatic heating).

In Fig. 4(a) we plot $W(\mathbf{k})$ in the plane $k_y = 0$, for $f_1 = f_2/\varphi$ and with all other parameters specified below Eq. (48). We also indicate the Fermi surface (dashed line) and schematically indicate the nonadiabatic region (shaded region), which surrounds the topological phase boundary (solid line). Since $\mu > 0$, band 1 is fully occupied in equilibrium. We therefore expect $\bar{\rho}_1(\mathbf{k}) \approx 1$ [see Eq. (27)] for all $\mathbf{k}$ away from the nonadiabatic region (where Landau-Zener tunneling can induce holes). We hence expect topological frequency conversion causes $\bar{P}(\mathbf{k})$ to approximately take value $h f_1 f_2[1 - \bar{\rho}_2(\mathbf{k})]$ within the red region of Fig. 4(a), value $-h f_1 f_2[1 - \bar{\rho}_2(\mathbf{k})]$ in the blue region, and value 0 in the white region.

In Fig. 4(b), we plot $\bar{P}(\mathbf{k})$ in the plane $k_y = 0$ in for parameters $f_1 = f_2/\varphi$ and $\tau = 51.6\,\mathrm{ps}$ [73]. The data shows clear signatures of topological frequency conversion, in the form of two "topological plateaux" of the Brillouin zone where $\bar{P}(\mathbf{k})$ takes positive and negative values, respectively. These plateaus coincide closely with the regions in Fig. 4(a) where $W(\mathbf{k}) = \pm 1$. $\bar{P}(\mathbf{k})$ approximately takes value $h f_1 f_2$ within the red plateau (away from the Weyl point), and value between 0 and $-h f_1 f_2$ within the blue plateau (close to the Weyl point).

We expect $\bar{P}(\mathbf{k})$ differs from $\pm h f_1 f_2$ in the topological plateaux due to the finite value of $\bar{\rho}_2(\mathbf{k}) - \bar{\rho}_1(\mathbf{k})$. To confirm this, we computed the time-averaged number of electrons per $\mathbf{k}$-point, $\langle \hat{n}(\mathbf{k}) \rangle \equiv \lim_{t\to\infty} \frac{1}{t} \int_0^t ds\, \mathrm{Tr}[\hat{n}\hat{\rho}(\mathbf{k}, s)]$, where $\hat{n} = \hat{c}_1^\dagger \hat{c}_1 + \hat{c}_2^\dagger \hat{c}_2$. Our expectation that $\bar{\rho}_1(\mathbf{k}) \approx 1$ implies that $2 - \langle \hat{n}(\mathbf{k}) \rangle$ should be a good proxy for $[\bar{\rho}_2(\mathbf{k}) - \bar{\rho}_1(\mathbf{k})]$ away from the nonadiabatic region. In Fig. 4(d) we plot $\langle \hat{n}(\mathbf{k}) \rangle$. Taken in combination with Figs. 4(ab), our data are thus consistent with $\bar{P}(\mathbf{k})$ taking value $\pm h f_1 f_2[\bar{\rho}_2(\mathbf{k}) - \bar{\rho}_1(\mathbf{k})]$ within the topological plateaux.

In addition to topological frequency conversion, the data in Fig. 4(b) also shows clear signatures of the two distinct mechanisms for dissipation that we identified in Sec. III C, i.e., momentum relaxation and nonadiabatic heating: $\bar{P}(\mathbf{k})$ takes large negative values within the nonadiabatic region, as we expect from nonadiabatic heating, and moderate negative values around the Fermi surface, as we expect from momentum relaxation.

Note also that the data in Fig. 4(d) are in good agreement with our prediction that in the regime $\tau \gg 1/\Omega$, the steady state band populations are effectively "smeared" versions of their equilibrium counterparts [see Eq. (27)]: The distribution in Fig. 4(d) clearly resembles a "smeared" version of the ellipsoid-profile that occurs in equilibrium [plotted in Fig. 4(c)].

Finally, the data in Figs. 4(cd) demonstrate how a nonzero value of the "Weyl cone tilt" $\mathbf{V}$ is needed to nonzero net rate of topological frequency conversion, $\bar{\eta}_0$, as we discussed in Sec. III B. The nonzero value of $\mathbf{V}$, which causes an ellipsoid-profile of $\langle \hat{n}(\mathbf{k}) \rangle$ in equilibrium [Fig. 4(c)], results in a "smeared ellipsoid" profile of $\langle \hat{n}(\mathbf{k}) \rangle$ in the steady state. As a result of this smeared ellipsoid profile, the region characterized by $W(\mathbf{k}) = 1$ has a larger volume in which $[\bar{\rho}_2(\mathbf{k}) - \bar{\rho}_1(\mathbf{k})] > 0$ ($\langle \hat{n}(\mathbf{k}) \rangle \leq 2$) than than the volume where $W(\mathbf{k}) = -1$, allowing for a nonzero value of $\bar{\eta}_0$.

C. Lissajous Conversion

We finally verify that the enhancement of $\bar{\eta}$ in the Lissajous regime (i.e., at commensurate frequencies) is due to the suppression of nonadiabatic heating. To this end, we plot in Fig. 5 $\bar{P}(\mathbf{k})$ for the parameters $\tau = 516\,\mathrm{ps}$ and $f_1 = 2f_2/3$ (a) and $f_1 = 2f_2/(3+\epsilon)$ (b). The two choices of f_1 are very close, but whereas the former choice of f_1 is commensurate with f_2, the latter choice is not. The negative values of $\bar{P}(\mathbf{k})$ within the nonadiabatic region (which we attribute to nonadiabatic heating), are much fainter in panel (a) than in panel (b). This is consistent with our expectation that nonadiabatic heating is indeed significantly suppressed for $f_1 = \frac{2}{3}f_2$ compared to $\frac{2}{3+\epsilon}f_2$.

We also compute the *total* dissipated power in the system due to both driving modes, $\bar{P}_{\mathrm{dis}}(\mathbf{k}) = -\lim_{t\to\infty}\int_0^t \frac{ds}{t}\,\mathrm{Tr}[\nabla\hat{H}(\mathbf{k},s)\hat{\rho}(\mathbf{k},s)]\cdot(\mathbf{E}_1(s)+\mathbf{E}_2(s))$, for the same parameters as in panels (a) and (b). $\bar{P}_{\mathrm{dis}}(\mathbf{k})$ measures the time-averaged rate of work done on electrons with wavevector $\mathbf{k}$ by the two driving modes in combination; hence it measures the total rate of dissipation, and is guaranteed to be positive due to the second law of thermodynamics. In Fig. 5(c) and (d) we plot $\bar{P}_{\mathrm{dis}}(\mathbf{k})$ for the parameter sets we considered in panels (a) and (b), respectively. While outside the nonadiabatic region, $\bar{P}(\mathbf{k})$ and $\bar{P}_{\mathrm{dis}}(\mathbf{k})$ effectively take the same values for the two frequency ratios, nonadiabatic heating is much weaker in panel (d) than in panel (c). The very different values of $\bar{\eta}$ at frequencies $f_1 = \frac{2}{3}f_2$ and $f_1 = \frac{2}{3+\epsilon}f_2$ must therefore be due to this suppression of nonadiabatic heating in the commensurate case.

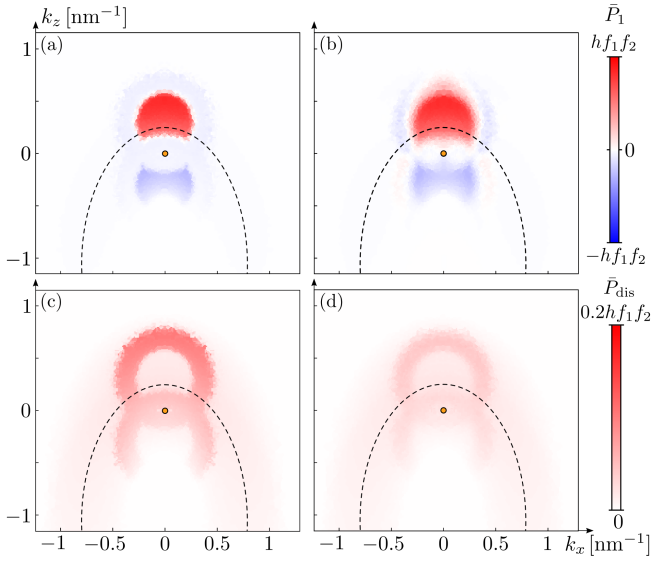

FIG. 5. Evidence of Lissajous conversion. (a,b): plot of $\bar{P}(\mathbf{k})$ in the plane $k_y = 0$ for parameters $\tau = 516\,\mathrm{ps}$, $f_1 = 2f_2/3$ (a), and $\tau = 516\,\mathrm{ps}$ and $f_1 = 2f_2/(3+\epsilon)$ (b). (c,d): total dissipation rate $\bar{P}_{\mathrm{tot}}(\mathbf{k})$ for the same parameters as depicted in panels (a) and (b),respectively. Note the different color scales used in panels (a,b) and (c,d).

V. CONDITIONS FOR FREQUENCY CONVERSION

There are several conditions that a Weyl material must satisfy to realize topological frequency conversion. The conditions can be grouped into the conditions that an individual Weyl node must satisfy (Sec. V A), the conditions on the global band structure and symmetry class of the system (Sec. V B), conditions on the driving (Sec. V C), and conditions on relaxation (Sec. V D).

A. Conditions on individual Weyl nodes

The rate of topological frequency conversion from Weyl node i is given by the ith term in the sum over Weyl nodes in Eq. (29): $\bar{\eta}_i = q_i h f_1 f_2 \int\frac{\mathrm{d}^3\mathbf{k}}{(2\pi)^3}[\bar{\rho}_2(\mathbf{k}) - \bar{\rho}_1(\mathbf{k})]W(\mathbf{k}-\mathbf{k}_i)$. Thus, Weyl point i can only contribute to frequency conversion if

$$\bar{\rho}_1(\mathbf{k}_i+\delta\mathbf{k}) \neq \bar{\rho}_2(\mathbf{k}_i+\delta\mathbf{k}) \quad \text{for } \delta\mathbf{k} \text{ within } \mathcal{B}_0. \tag{50}$$

Therefore only the Weyl nodes sufficiently near the Fermi energy can contribute to topological frequency conversion. If a Weyl node is too far from the Fermi energy, the two touching bands are either both full or empty within a distance $\sim eA/\hbar$ from the Weyl node, implying $\bar{\rho}_1(\mathbf{k}_i+\delta\mathbf{k}) \approx \bar{\rho}_2(\mathbf{k}_i+\delta\mathbf{k})$ for $\delta\mathbf{k}_i$ within $\mathcal{B}_0$.

For the most natural case where each of the two modes contains only a single harmonic, $W(\mathbf{k}) = -W(-\mathbf{k})$, as is also evident in Figs. 2(c) and 4(a). For Weyl point i to contribute to frequency conversion, $\bar{\rho}_1(\mathbf{k})$ or $\bar{\rho}_2(\mathbf{k})$ must hence break inversion symmetry around $\mathbf{k}_i$. Specifically

$$\bar{\rho}_\alpha(\mathbf{k}_i+\delta\mathbf{k}) \neq \bar{\rho}_\alpha(\mathbf{k}_i-\delta\mathbf{k}) \quad \text{for } \delta\mathbf{k} \text{ within } \mathcal{B}_0. \tag{51}$$

This constitutes our second condition. This symmetry breaking can be achieved with a nonzero value of the Weyl cone tilt, $\mathbf{v}$ [see Eq. (1)], as we demonstrated in our numerical simulations (Sec. IV).

B. Condition on symmetry class

We now identify the symmetries a Weyl semimetal must break to support topological frequency conversion.

The two symmetries that are central to the Weyl semimetals are the inversion and the time-reversal symmetry [12]; at least one of these symmetries must be broken for the Weyl nodes to exist. Both inversion and time-reversal symmetry results in inversion-symmetric energy bands, $\varepsilon_\alpha(\mathbf{k}) = \varepsilon_\alpha(-\mathbf{k})$ (with α denoting the band index after indexing them according to their energy). Thus, for both symmetries, a Weyl point at wavevector $\mathbf{k}$ implies the existence of a Weyl point at wavevector $-\mathbf{k}$. The conjugate Weyl nodes at $\mathbf{k}$ and $-\mathbf{k}$ have equal charges for time-reversal symmetric Weyl semimetals, and opposite

charges for inversion-symmetric Weyl semimetals [12]. We expect the steady-state to approximately inherit the same inversion symmetry, such that $\bar{\rho}_\alpha(\mathbf{k}) = \bar{\rho}_\alpha(-\mathbf{k})$. For the most natural case where modes 1 and 2 each contain a single harmonic, $W(\mathbf{k}) = -W(-\mathbf{k})$. Hence the contributions to $\bar{\eta}_0$ from symmetry-conjugate nodes cancel out for Weyl semimetals with time-reversal symmetry, but not for Weyl semimetals with inversion symmetry.

We conclude that broken time-reversal symmetry is required for topological frequency conversion, while inversion symmetry does not need to be broken. Other crystal symmetries, such as reflection and discrete rotation symmetry, do also not preclude frequency conversion, since the incoming modes (and hence $W(\mathbf{k})$) can be configured in a way that breaks these symmetries. Hence magnetic Weyl semimetals, such as Co_3Sn_2S or Co_2MnGa [49, 51], intrinsically support topological frequency conversion, while non-magnetic Weyl semimetals (such as TaAs) require an externally-provided time-reversal symmetry breaking. Such symmetry breaking can e.g. be achieved with a current bias or externally applied magnetic field.

C. Condition on driving

Next, we identify the conditions that the driving amplitudes and frequencies must satisfy to support frequency conversion for a given Weyl semimetal.

Sec. III C 2 concluded that the dynamics of electrons is non-adiabatic within a distance d_0 from the boundary $\mathcal{B}_0$, where $d_0 \sim \sqrt{\frac{eE}{\hbar v_0}}$, and v_0 is the smallest singular value of the matrix R in Eq. (1) [see Eq. (36)]. For a nonzero number electrons to act as frequency converters, d_0 must hence be smaller than the linear dimension of $\mathcal{B}_0$, which we estimate to be of order $eA/\hbar$. These considerations imply that $E \gg \frac{\hbar\Omega^2}{ev_0}$ is required for frequency conversion. Equivalently, we require that the characteristic intensity, I, satisfies

$$I \gg \frac{\hbar^2\Omega^4}{2c\varepsilon_0 v_0^2}. \tag{52}$$

Hence, "steep" Weyl points (i.e., Weyl points with large v_0) are most useful for frequency conversion, as they support topological frequency conversion at lower intensities.

Weyl points in known compounds support topological frequency conversion at experimentally accessible parameters: for example, TaAs has Weyl points for which $v_0 \sim 10^5\,\mathrm{m/s}$ [71, 72] At frequency $\Omega \sim 2\pi\,\mathrm{THz}$, we hence expect these Weyl points can support topological frequency conversion at moderate intensities of order $100\,\mathrm{W/mm^2}$ and above.

Finally, we require that the bandwidth of the bands containing the Weyl node be larger than the driving frequency; otherwise, driving cannot be considered adiabatic anywhere in the system. This puts an upper limit for the frequencies that could achieve frequency conversion in a given Weyl semimetal. As an example, for TaAs the characteristic band gap between Weyl points is of order 20 meV [71], corresponding to a maximum frequency limit of $\sim 5\,\mathrm{THz}$.

D. Condition on relaxation

A final condition for amplification, is that the rate of topological energy conversion, $\bar{\eta}_0$, must overcome the (negative) rate of dissipation, $\bar{\eta}_{\mathrm{dis}}$. Our analysis and numerical simulations identified two sources of dissipation: momentum relaxation (η_{mr}) and nonadiabatic heating (η_{na}): $\eta_{\mathrm{dis}} = \eta_{\mathrm{mr}} + \eta_{\mathrm{na}}$. Amplification of mode 1 thus requires

$$\bar{\eta}_0 + \eta_{\mathrm{mr}} + \eta_{\mathrm{na}} > 0, \tag{53}$$

In Sec. III C 2 we concluded that the *gross* rate of topological frequency conversion, η_{gross} (i.e., the rate that results when not taking into account cancellation between electrons that convert energy in opposite directions), can only exceed η_{na} if $\tau \gtrsim 1/\Omega$. Since the net rate of topological frequency conversion, $\bar{\eta}_0$, is just a small fraction of η_{gross}, and since energy is also lost to momentum relaxation, we hence expect net amplification ($\bar{\eta} > 0$) can only be achieved when

$$\tau \gg 1/\Omega \tag{54}$$

The phenomenological discussion in Sec. III C 2 shows that $\eta_{\mathrm{na}} \propto (1 - e^{-\Gamma\Delta t})$ where Δt denotes the characteristic time between instances where a given wavevector $\mathbf{k}$ is taken to the Weyl point by the applied drive ($\mathbf{k} \to \mathbf{k} + e\mathbf{A}(t)/\hbar$). Here Δt is significantly smaller for Lissajous conversion (highly rational frequency ratios) than for incommensurate frequency ratios. Thus, the threshold for net amplification is significantly lower at commensurate frequencies. Indeed, in our simulations, a small adjustment of f_1 from $2f_2/(3+\epsilon)$ to $2f_2/3$ lowered the amplification threshold from above 1200 ps to $\sim 300\,\mathrm{ps}$.

Our quoted values in Sec. III provide an example of how to estimate the break-even relaxation rate. For intensity $6\,\mathrm{kW/mm^2}$ and $\Omega \sim 2\pi\mathrm{THz}$, we estimated $\eta_{\mathrm{gross}} \sim 500\,\mathrm{kW/mm^3}$. The net rate $\bar{\eta}_0$ will be only a fraction of this value. For the same parameters, and with isotropic band gap matrix R of order $5{\cdot}10^5\,\mathrm{m/s}$ and Fermi surface area $0.06\,\mathrm{\AA}^{-2}$, we found $\eta_{\mathrm{mr}} \sim 5\cdot10^{-8}\,\mathrm{kJ/mm^3}\tau$, and $\eta_{\mathrm{na}} \sim 5\cdot10^{-8}\,\mathrm{kJ/mm^3}\tau$ (for incommensurate frequencies) or $3.5\cdot10^{-9}\,\mathrm{kJ/mm^3}\tau$ (for Lissajous conversion at frequency ratio 2/3). Hence, we expect topological frequency conversion can exceed the rate of dissipation when τ are several times larger than 100ps. We moreover expect the threshold to be significantly lower for Lissajous conversion (i.e. commensurate frequencies), than for incommensurate frequencies. This is in good agreement with our data in Fig. 1(b) which indicate that τ

must exceed 300 ps in order to achieve net frequency conversion in the Lissajous regime for the parameters above, and 1000ps for incommensurate frequencies.

The different scaling behaviors of dissipation and topological frequency conversion point toward the parameter regimes beneficial for amplification.

First, note that (at a fixed area of the Fermi surface), $\eta_{\rm mr}$ scales linearly with intensity I, while $\eta_{\rm na}$ and $\eta_{\rm gross}$ scales as $I^{3/2}$ (specifically, $\eta_{\rm na} \sim I^{3/2}$ in the Lissajous regime) [see Eqs. (34),(37), and (30)]. Thus, we expect that the relative contribution of $\eta_{\rm mr}$ decreases at high intensity, while the ratio of $\eta_{\rm na}$ and $\eta_{\rm gross}$ remains fixed, implying that frequency conversion becomes more efficient at higher intensities.

Second, for a given intensity, the topological frequency conversion rate scales as $1/\Omega$, while $\eta_{\rm na}$ scales as $1/\Omega^3$ (for incommensurate frequencies) or $1/\Omega^2$ (for commensurate frequencies). Similarly, momentum relaxation scales as $1/\Omega^2$. Thus, we expect amplification is most easily reached at the top of the frequency range that supports topological frequency conversion, given the driving intensity and band structure of the system.

The requirements on the relaxation rate pose the biggest current challenge to realizing topological frequency conversion. Relaxation times in known Weyl semimetals have been reported to be in the range $0.25-3$ps [37–39, 41], although transient signatures with lifetimes above 100 [41, 42] and 1000 [43] ps have also been reported in some compounds. Thus further improvements in the quality of materials are needed to fulfill the requirements of topological frequency conversation in the practically interesting THz range.

VI. DISCUSSION

In this paper, we showed that Weyl semimetals can efficiently convert energy between two driving modes, through the mechanism of topological frequency conversion [31]. This effect makes Weyl semimetals promising media for THz and possibly even infrared amplification. Our analysis shows that real materials (such as TaAs) support topological frequency conversion at THz frequencies in experimentally accessible intensity ranges ($\sim 100\,\mathrm{W/mm^2}$). Topological frequency conversion is supported both for incommensurate frequencies and commensurate frequencies, but is most efficient in the latter case, due to the mechanism of Lissajous conversion. Our numerics and estimates focused on topological frequency conversion in the THz regime, where there is the biggest need for new photonic control elements, but the effect may also be supported at other frequency ranges.

The primary obstacle to Weyl semimetals operating as topological frequency converters is driving-induced heating. Heating both wastes energy from the beams we would like to amplify, and may even damage the material. Phonons, interactions and impurities all lead to electron relaxation processes which cause this heating.

Through phenomenological arguments and numerical simulations, we identified two important mechanisms for dissipation: momentum relaxation and nonadiabatic heating. Momentum relaxation occurs when electrons near the Fermi surface relax their energy by changing their momentum, and which is common to all irradiated materials. Nonadiabatic heating emerges when electrons undergo Landau-Zener transitions between the valence and the conduction band. This mechanism is particularly relevant in topological semimetals, due to the existence of gap-closing points in these materials. Even so, nonadiabatic heating is strongly suppressed in the Lissajous regime, which makes it much preferred for amplification.

In our simulations and phenomenological discussion, relaxation was parameterized through a single relaxation time, τ. In particular, we took electron-hole recombination, and intra-band momentum relaxation (which is supported by phonons) to have the same characteristic rates. Needless to say this treatment could be made more realistic by considering separate relaxation rates for these processes, as suggested by experiments [39, 41, 42]. Nonetheless, we believe our simple dynamical model captures the conditions for amplification.

To achieve amplification, where energy gain due to topological frequency conversion exceeds the loss due to dissipation, the characteristic relaxation time τ must be sufficiently long. To limit non-adiabatic heating as well as momentum relaxation we need $\tau f \gg 1$. This condition was clearly evident in our simulations: even for optimal parameters, and in the Lissajous regime, breakeven was only reached when $1/\tau \gtrsim 300 f$,(for incommensurate frequencies, amplification required $\tau f > 1000$). So far, τ's were reported in the range $0.25-5\,\mathrm{ps}$ [37–39] in pump-probe experiments. This suggests net amplification of continuous-wave THz frequencies is currently beyond reach. That said, transient experimental signatures with $\tau > 100\,\mathrm{ps}$ have been seen in Weyl semimetals [41, 42], emphasizing that a more discriminating analysis may reveal a broader amplification regime.

Notwithstanding, signatures of topological frequency conversion effect could be observed even if the relaxation time is too short to allow for amplification. That is because the direction of energy conversion of a Weyl semimetal driven bichromatically by two circularly-polarized modes is determined by the product of the two mode's polarizations. Hence a reversal of the circular polarization of either mode should will lead to an increase in the output intensity of one mode, and a decrease for the other mode. This topological effect could be accessed experimentally.

Furthermore, we can suggest several strategies to approach the amplification regime. Commensurate frequency conversion, i.e. Lissajous conversion, already provides a dramatic improvement by suppressing nonadiabatic effects by an order of magnitude. Momentum relaxation is harder to control. Note, however, that momentum relaxation energy loss scales linearly with radiation intensity, I. In contrast, topological energy conver-

sion (and nonadiabatic heating) scale as $I^{3/2}$. Therefore the relative significance of momentum relaxation should decrease at larger intensities. Moreover, at a given intensity, topological frequency conversion scales inversely with the driving frequency, f, while dissipative energy absorption decreases as f^{-2} (specifically, $\eta_{\rm na} \sim f^{-2}$ in the Lissajous conversion regime). The amplification threshold of τf will therefore be lower at higher frequencies.

The regime of higher intensities and frequencies puts different constraints on the materials needed for topological frequency conversion. Larger intensities induce heating which may cause material damage. This problem, however, could possibly be circumvented by using pulsed lasers instead of continuous wave beams: by allowing the system to dissipate heat between pulses, such a scheme would allow us to reach the high-intensity regime without causing material damage. This way the large-amplitude regime required for frequency conversion could be realized while allowing time for the system to dissipate absorbed heat between pulses even if relaxation times are short. In addition to these considerations, materials with a steeper velocity makes realizing the large frequency regime easier, as the velocity at the Weyl point is the "coupling constant" that converts the electric-field amplitude into an energy scale.

Weyl nodes need to be located near the Fermi surface to support topological frequency conversion, and moreover need to be surrounded by an asymmetric electron distribution, in order to ensure an imbalance in the numbers of electrons that convert energy at opposite rates. Optimal imbalance can be reached in the presence of a "Weyl cone tilt", and through appropriate tuning of the chemical potential. Additionally, our analysis indicates that time-reversal symmetry needs to be broken to acheive frequency conversion. Hence, we expect magnetic Weyl semimetals, such as Co_3Sn_2S or Co_2MnGa [49, 51] are best-suited for topological frequency conversion.

Topological frequency conversion could also be achieved in non-magnetic Weyl semimetals, or even be enhanced in magnetic Weyl semimetals, by "priming" the particle distribution into an out-of-equilibrium state. Such priming could e.g. be achived by driving the system with ultrashort laser pulses or with a DC current, and would create a transient state more suited for frequency conversion than the steady states we have considered in this work. Similarly, purification of the material, alongside bath or substrate engineering are other potentially important directions for realizing amplification by suppressing dissipation. Indeed, these research directions are also important for the general nonlinear response of Weyl semimetals (e.g., chiral photogalvanic effect) [19].

Acknowledgements — We thank Mark Rudner, Prineha Narang, Chris Ciccarino, and N. Peter Armitage for valuable discussions. FN gratefully acknowledges the support of the European Research Council (ERC) under the European Union Horizon 2020 Research and Innovation Programme (Grant Agreement No. 678862) and the Villum Foundation. IM was supported by the Materials Sciences and Engineering Division, Basic Energy Sciences, Office of Science, U.S. Department of Energy. GR is grateful for support from the Simons Foundation as well as support from the NSF DMR grant number 1839271. This work is supported by ARO MURI Grant No. W911NF-16-1-0361, and was performed in part at Aspen Center for Physics, which is supported by National Science Foundation grant PHY-1607611.

[1] H. Nielsen and M. Ninomiya, Absence of neutrinos on a lattice: (ii). intuitive topological proof, Nuclear Physics B **193**, 173 (1981).

[2] H. Nielsen and M. Ninomiya, A no-go theorem for regularizing chiral fermions, Physics Letters B **105**, 219 (1981).

[3] X. Wan, A. M. Turner, A. Vishwanath, and S. Y. Savrasov, Topological semimetal and fermi-arc surface states in the electronic structure of pyrochlore iridates, Phys. Rev. B **83**, 205101 (2011).

[4] D. T. Son and B. Z. Spivak, Chiral anomaly and classical negative magnetoresistance of weyl metals, Phys. Rev. B **88**, 104412 (2013).

[5] A. C. Potter, I. Kimchi, and A. Vishwanath, Quantum oscillations from surface fermi arcs in weyl and dirac semimetals, Nature Communications **5**, 5161 (2014).

[6] Y. Baum, E. Berg, S. A. Parameswaran, and A. Stern, Current at a distance and resonant transparency in weyl semimetals, Phys. Rev. X **5**, 041046 (2015).

[7] S.-M. Huang, S.-Y. Xu, I. Belopolski, C.-C. Lee, G. Chang, B. Wang, N. Alidoust, G. Bian, M. Neupane, C. Zhang, S. Jia, A. Bansil, H. Lin, and M. Z. Hasan, A weyl fermion semimetal with surface fermi arcs in the transition metal monopnictide taas class, Nature Communications **6**, 7373 (2015).

[8] B. Q. Lv, H. M. Weng, B. B. Fu, X. P. Wang, H. Miao, J. Ma, P. Richard, X. C. Huang, L. X. Zhao, G. F. Chen, Z. Fang, X. Dai, T. Qian, and H. Ding, Experimental discovery of weyl semimetal taas, Phys. Rev. X **5**, 031013 (2015).

[9] H. Weng, C. Fang, Z. Fang, B. A. Bernevig, and X. Dai, Weyl semimetal phase in noncentrosymmetric transition-metal monophosphides, Phys. Rev. X **5**, 011029 (2015).

[10] S.-Y. Xu, I. Belopolski, D. S. Sanchez, C. Zhang, G. Chang, C. Guo, G. Bian, Z. Yuan, H. Lu, T.-R. Chang, P. P. Shibayev, M. L. Prokopovych, N. Alidoust, H. Zheng, C.-C. Lee, S.-M. Huang, R. Sankar, F. Chou, C.-H. Hsu, H.-T. Jeng, A. Bansil, T. Neupert, V. N. Strocov, H. Lin, S. Jia, and M. Z. Hasan, Experimental discovery of a topological weyl semimetal state in tap, Science Advances **1**, 6 (2015).

[11] B. Yan and C. Felser, Topological materials: Weyl semimetals, Annual Review of Condensed Matter Physics **8**, 337 (2017).

[12] N. P. Armitage, E. J. Mele, and A. Vishwanath, Weyl and dirac semimetals in three-dimensional solids, Rev. Mod. Phys. **90**, 015001 (2018).

[13] S. Parkin, X. Jiang, C. Kaiser, A. Panchula, K. Roche, and M. Samant, Magnetically engineered spintronic sensors and memory, Proceedings of the IEEE **91**, 661 (2003).

[14] C. Shekhar, A. K. Nayak, Y. Sun, M. Schmidt, M. Nicklas, I. Leermakers, U. Zeitler, Y. Skourski, J. Wosnitza, Z. Liu, Y. Chen, W. Schnelle, H. Borrmann, Y. Grin, C. Felser, and B. Yan, Extremely large magnetoresistance and ultrahigh mobility in the topological weyl semimetal candidate nbp, Nature Physics **11**, 645 (2015).

[15] G. B. Osterhoudt, L. K. Diebel, M. J. Gray, X. Yang, J. Stanco, X. Huang, B. Shen, N. Ni, P. J. W. Moll, Y. Ran, and K. S. Burch, Colossal mid-infrared bulk photovoltaic effect in a type-i weyl semimetal, Nature Materials **18**, 471 (2019).

[16] L. Wu, S. Patankar, T. Morimoto, N. L. Nair, E. Thewalt, A. Little, J. G. Analytis, J. E. Moore, and J. Orenstein, Giant anisotropic nonlinear optical response in transition metal monopnictide weyl semimetals, Nature Physics **13**, 350 (2016).

[17] T. Morimoto, S. Zhong, J. Orenstein, and J. E. Moore, Semiclassical theory of nonlinear magneto-optical responses with applications to topological dirac/weyl semimetals, Phys. Rev. B **94**, 245121 (2016).

[18] C.-K. Chan, N. H. Lindner, G. Refael, and P. A. Lee, Photocurrents in weyl semimetals, Phys. Rev. B **95**, 041104 (2017).

[19] F. de Juan, A. G. Grushin, T. Morimoto, and J. E. Moore, Quantized circular photogalvanic effect in weyl semimetals, Nature Communications **8**, 15995 (2017).

[20] N. Sirica, R. I. Tobey, L. X. Zhao, G. F. Chen, B. Xu, R. Yang, B. Shen, D. A. Yarotski, P. Bowlan, S. A. Trugman, J.-X. Zhu, Y. M. Dai, A. K. Azad, N. Ni, X. G. Qiu, A. J. Taylor, and R. P. Prasankumar, Tracking ultrafast photocurrents in the weyl semimetal taas using thz emission spectroscopy, Phys. Rev. Lett. **122**, 197401 (2019).

[21] T. Oka and S. Kitamura, Floquet engineering of quantum materials, Annual Review of Condensed Matter Physics **10**, 387 (2019).

[22] K. Takasan, T. Morimoto, J. Orenstein, and J. E. Moore, Current-induced second harmonic generation in inversion-symmetric dirac and weyl semimetals (2020), arXiv:2007.08887 [cond-mat.mes-hall].

[23] R. M. A. Dantas, Z. Wang, P. Surówka, and T. Oka, Nonperturbative topological current in weyl and dirac semimetals in laser fields (2020), arXiv:2008.04331 [cond-mat.mes-hall].

[24] V. Khemani, A. Lazarides, R. Moessner, and S. L. Sondhi, Phase structure of driven quantum systems, Phys. Rev. Lett. **116**, 250401 (2016).

[25] D. V. Else, B. Bauer, and C. Nayak, Floquet time crystals, Phys. Rev. Lett. **117**, 090402 (2016).

[26] T. Oka and H. Aoki, Photovoltaic hall effect in graphene, Phys. Rev. B **79**, 081406 (2009).

[27] N. H. Lindner, G. Refael, and V. Galitski, Floquet topological insulator in semiconductor quantum wells, Nat. Phys. **7**, 490 (2011).

[28] M. S. Rudner, N. H. Lindner, E. Berg, and M. Levin, Anomalous edge states and the bulk-edge correspondence for periodically driven two-dimensional systems, Phys. Rev. X **3**, 031005 (2013).

[29] P. Titum, E. Berg, M. S. Rudner, G. Refael, and N. H. Lindner, Anomalous floquet-anderson insulator as a nonadiabatic quantized charge pump, Phys. Rev. X **6**, 021013 (2016).

[30] F. Nathan, D. Abanin, E. Berg, N. H. Lindner, and M. S. Rudner, Anomalous floquet insulators, Phys. Rev. B **99**, 195133 (2019).

[31] I. Martin, G. Refael, and B. Halperin, Topological frequency conversion in strongly driven quantum systems, Phys. Rev. X **7**, 041008 (2017).

[32] M. H. Kolodrubetz, F. Nathan, S. Gazit, T. Morimoto, and J. E. Moore, Topological floquet-thouless energy pump, Phys. Rev. Lett. **120**, 150601 (2018).

[33] F. Nathan, R. Ge, S. Gazit, M. S. Rudner, and M. Kolodrubetz, Quasiperiodic Floquet-Thouless energy pump, arXiv (2020), 2010.11485.

[34] D. M. Long, P. J. D. Crowley, and A. Chandran, Nonadiabatic topological energy pumps with quasiperiodic driving, Phys. Rev. Lett. **126**, 106805 (2021).

[35] E. Boyers, P. J. D. Crowley, A. Chandran, and A. O. Sushkov, Exploring 2d synthetic quantum hall physics with a quasiperiodically driven qubit, Phys. Rev. Lett. **125**, 160505 (2020).

[36] D. Malz and A. Smith, Topological two-dimensional floquet lattice on a single superconducting qubit, Phys. Rev. Lett. **126**, 163602 (2021).

[37] Y. M. Dai, J. Bowlan, H. Li, H. Miao, S. F. Wu, W. D. Kong, P. Richard, Y. G. Shi, S. A. Trugman, J.-X. Zhu, H. Ding, A. J. Taylor, D. A. Yarotski, and R. P. Prasankumar, Ultrafast carrier dynamics in the large-magnetoresistance material wte_2, Phys. Rev. B **92**, 161104 (2015).

[38] C. P. Weber, E. Arushanov, B. S. Berggren, T. Hosseini, N. Kouklin, and A. Nateprov, Transient reflectance of photoexcited cd3as2, *Applied Physics Letters*, Applied Physics Letters **106**, 231904 (2015).

[39] C. P. Weber, B. S. Berggren, M. G. Masten, T. C. Ogloza, S. Deckoff-Jones, J. Madéo, M. K. L. Man, K. M. Dani, L. Zhao, G. Chen, J. Liu, Z. Mao, L. M. Schoop, B. V. Lotsch, S. S. P. Parkin, and M. Ali, Similar ultrafast dynamics of several dissimilar dirac and weyl semimetals, Journal of Applied Physics **122**, 223102 (2017).

[40] B. Cheng, T. Schumann, S. Stemmer, and N. P. Armitage, Probing charge pumping and relaxation of the chiral anomaly in a dirac semimetal, Science Advances **7**, eabg0914 (2021), https://www.science.org/doi/pdf/10.1126/sciadv.abg0914.

[41] Y. Ishida, H. Masuda, H. Sakai, S. Ishiwata, and S. Shin, Revealing the ultrafast light-to-matter energy conversion before heat diffusion in a layered dirac semimetal, Phys. Rev. B **93**, 100302 (2016).

[42] J. Liu, L. Cheng, D. Zhao, X. Chen, H. Sun, Z. Li, X. Wang, J.-X. Zhu, and E. E. M. Chia, Quenching of the relaxation pathway in the weyl semimetal taas, Phys. Rev. B **102**, 064307 (2020).

[43] M. M. Jadidi, M. Kargarian, M. Mittendorff, Y. Aytac, B. Shen, J. C. König-Otto, S. Winnerl, N. Ni, A. L. Gaeta, T. E. Murphy, and H. D. Drew, Nonlinear optical control of chiral charge pumping in a topological weyl semimetal, Phys. Rev. B **102**, 245123 (2020).

[44] A Weyl point can only disappear when this continuous motion causes it to merge and annihilate with another Weyl point. The two annihilating Weyl points must have opposite chiralities (see below). Under such an elimina-

tion, one of the eigenvalues of R will decrease to zero. Such an elimination is always possible, since the chiralities of all Weyl points in any given gap must sum to zero [1]. Conversely, Weyl points can be "nucleate" pairwise under a smooth change of system parameters.

[45] S.-Y. Xu, I. Belopolski, N. Alidoust, M. Neupane, G. Bian, C. Zhang, R. Sankar, G. Chang, Z. Yuan, C.-C. Lee, S.-M. Huang, H. Zheng, J. Ma, D. S. Sanchez, B. Wang, A. Bansil, F. Chou, P. P. Shibayev, H. Lin, S. Jia, and M. Z. Hasan, Discovery of a weyl fermion semimetal and topological fermi arcs, Science **349**, 613 (2015).

[46] D.-F. Xu, Y.-P. Du, Z. Wang, Y.-P. Li, X.-H. Niu, Q. Yao, D. Pavel, Z.-A. Xu, X.-G. Wan, and D.-L. Feng, Observation of fermi arcs in non-centrosymmetric weyl semi-metal candidate NbP, Chinese Physics Letters **32**, 107101 (2015).

[47] S.-Y. Xu, N. Alidoust, I. Belopolski, Z. Yuan, G. Bian, T.-R. Chang, H. Zheng, V. N. Strocov, D. S. Sanchez, G. Chang, C. Zhang, D. Mou, Y. Wu, L. Huang, C.-C. Lee, S.-M. Huang, B. Wang, A. Bansil, H.-T. Jeng, T. Neupert, A. Kaminski, H. Lin, S. Jia, and M. Zahid Hasan, Discovery of a weyl fermion state with fermi arcs in niobium arsenide, Nature Physics **11**, 748 (2015).

[48] X. Huang, L. Zhao, Y. Long, P. Wang, D. Chen, Z. Yang, H. Liang, M. Xue, H. Weng, Z. Fang, X. Dai, and G. Chen, Observation of the chiral-anomaly-induced negative magnetoresistance in 3d weyl semimetal taas, Phys. Rev. X **5**, 031023 (2015).

[49] Q. Xu, E. Liu, W. Shi, L. Muechler, J. Gayles, C. Felser, and Y. Sun, Topological surface fermi arcs in the magnetic weyl semimetal $co_3sn_2s_2$, Phys. Rev. B **97**, 235416 (2018).

[50] I. Belopolski, K. Manna, D. S. Sanchez, G. Chang, B. Ernst, J. Yin, S. S. Zhang, T. Cochran, N. Shumiya, H. Zheng, B. Singh, G. Bian, D. Multer, M. Litskevich, X. Zhou, S.-M. Huang, B. Wang, T.-R. Chang, S.-Y. Xu, A. Bansil, C. Felser, H. Lin, and M. Z. Hasan, Discovery of topological weyl fermion lines and drumhead surface states in a room temperature magnet, Science **365**, 1278 (2019).

[51] P. Swekis, A. S. Sukhanov, Y.-C. Chen, A. Gloskovskii, G. H. Fecher, I. Panagiotopoulos, J. Sichelschmidt, V. Ukleev, A. Devishvili, A. Vorobiev, D. S. Inosov, S. T. B. Goennenwein, C. Felser, and A. Markou, Magnetic and electronic properties of weyl semimetal co2mnga thin films, Nanomaterials **11**, 251 (2021).

[52] Note that q is invariant under continuous basis transformations and coordinate system rotations, and hence takes the same value for any choice of basis for the two touching bands, and for any coordinate system.

[53] See below for the conditions for this result, and see Appendix B for derivation.

[54] Not taking into account nonadiabatic effects.

[55] F. Nathan, I. Martin, and G. Refael, Topological frequency conversion in a driven dissipative quantum cavity, Phys. Rev. B **99**, 094311 (2019).

[56] We could also have formulated the problem in the "comoving frame", by introducing the time-dependent wavevector $\mathbf{h}(t) = \mathbf{k} + e\mathbf{A}(t)/\hbar$. The Hamiltonian that results from this transformation is not block-diagonal in $\mathbf{h}$, but is given by $\tilde{H}(\mathbf{h}, t) = H(\mathbf{h}) - i\frac{e}{\hbar}\mathbf{E}(t)\cdot\nabla_{\mathbf{h}}$. However, the form in Eq. (6) is more convenient for our purpose. The transformation from $\tilde{H}$ to H corresponds to a time-dependent gauge transformation in real space.

[57] Here shifts in the time-origin correspond to shifts of $\mathbf{A}(t)$ by some constant displacement $\mathbf{A}_0$. Such shifts are equivalent to gauge transformations and hence do not affect the physical behavior of the system.

[58] This result can be derived from the equation of motion of the energy density in the system: $dE/dt = \int \frac{\mathrm{d}^3\mathbf{k}}{(2\pi)^3}\langle\partial_t\hat{H}(\mathbf{k},t)\rangle$. Using that $\partial_t\hat{H}(\mathbf{k},t) = \frac{e}{\hbar}\mathbf{E}(t)\cdot\nabla\hat{H}(\mathbf{k},t)$ along with the expression for the current density, we find $dE/dt = -(\mathbf{E}_1(t)\cdot\mathbf{j}(t) + \mathbf{E}_1(t)\cdot\mathbf{j}(t))$. We thus identify $-\mathbf{E}_i(t)\cdot\mathbf{j}(t)$ as the energy flow into the system from mode i per unit volume.

[59] This condition of adiabaticity corresponds to the condition of a "weak force" that we alluded to in Sec. I.

[60] For example, this definition, Eq. 18 implies $\mathrm{Tr}(\hat{\rho}(\mathbf{k},t)\hat{c}_i^\dagger\hat{c}_j) = \langle\hat{c}_{i,\mathbf{k}}^\dagger(t)\hat{c}_{j,\mathbf{k}}(t)\rangle$ where $\hat{c}_{i,\mathbf{k}}^\dagger$ creates a fermion in orbital i with crystal momentum $\mathbf{k}$.

[61] F. Nathan and M. S. Rudner, Universal lindblad equation for open quantum systems, Phys. Rev. B **102**, 115109 (2020).

[62] Here $\|\cdot\|$ can for example denote the spectral norm for linear operators.

[63] P. M. W. French, The generation of ultrashort laser pulses, Reports on Progress in Physics **58**, 169 (1995).

[64] When $\mathbf{A}_i(t)$ contains higher harmonics, $W(\mathbf{k})$ can potentially break this inversion antisymmetry. However, even for such cases $\int \mathrm{d}^3\mathbf{k}W(\mathbf{k})$ still vanishes implying that the regions of reciprocal space characterized by conversion rates hf_1f_2 and $-hf_1f_2$ have equal net volumes.

[65] L. D. Landau, Zur theorie der energieübertragung. ii, Physics of the Soviet Union **2**, 46 (1932).

[66] C. Zener and R. H. Fowler, Non-adiabatic crossing of energy levels, Proceedings of the Royal Society of London. Series A, Containing Papers of a Mathematical and Physical Character **137**, 696 (1932).

[67] We do not exclude the possibility that dynamics are still be adiabatic for some $\mathbf{k}$-points where $\min_t|\mathbf{k}+e\mathbf{A}(t)/\hbar| < d_0$. Our condition above may thus overestimate the extent of $\mathcal{V}_{\mathrm{na}}$, and hence also η_{na}.

[68] This regime typically does not occur for the limit we consider where $\Gamma \ll \Omega$. However, it may arise for rapid relaxation.

[69] In principle, gap-closing events may occur more often if $e\mathbf{A}(t)/\hbar$ returns to within a distance d_0 from the same point over a time-interval shorter than Δt (as occurs for near commensurate-frequencies, or if p/q is close to some rational fraction which involves smaller integers). In any case, qT_1 provides an upper bound for Δt.

[70] We estimate the accuracy of our computed value of $\bar{\eta}$ using the standard deviation of the values of $\bar{\eta}$ that result from restricting the integral random subsets of the sampled $\mathbf{k}$-points.

[71] F. Arnold, M. Naumann, S.-C. Wu, Y. Sun, M. Schmidt, H. Borrmann, C. Felser, B. Yan, and E. Hassinger, Chiral weyl pockets and fermi surface topology of the weyl semimetal taas, Phys. Rev. Lett. **117**, 146401 (2016).

[72] B. J. Ramshaw, K. A. Modic, A. Shekhter, Y. Zhang, E.-A. Kim, P. J. W. Moll, M. D. Bachmann, M. K. Chan, J. B. Betts, F. Balakirev, A. Migliori, N. J. Ghimire, E. D. Bauer, F. Ronning, and R. D. McDonald, Quantum limit transport and destruction of the weyl nodes in taas, Nature Communications **9**, 2217 (2018).

[73] We choose this value of τ for illustrative purposes, to make the contributions to $\bar{P}(\mathbf{k})$ from topological frequency conversion and dissipation visible on the same energy scale.
[74] Since he electric field from mode i only depends on ϕ_i, $\boldsymbol{\epsilon}_i(\phi)$ only depends on the ith component of $\phi = (\phi_1, \phi_2)$. We choose the notation $\boldsymbol{\epsilon}(\phi)$ for convenience.
[75] Here we take the inner product in operator space to be the Hilbert-Schmidt product, $(\hat{A}, \hat{B}) = \mathrm{Tr}[\hat{A}^\dagger \hat{B}]$.
[76] M. V. Berry, Quantum phase corrections from adiabatic iteration, Proceedings of the Royal Society of London. A. Mathematical and Physical Sciences **414**, 31 (1987).
[77] H. P. Breuer and F. Petruccione, *The theory of open quantum systems* (Oxford University Press, Great Clarendon Street, 2002).
[78] C. Gardiner and P. Zoller, *Quantum Noise* (Springer-Verlag Berlin Heidelberg, 2004).
[79] This follows using the chain rule along with $|\partial_t \varepsilon_\alpha| \leq |\partial_t H| \leq \lambda \delta \varepsilon^2$.
[80] This follows since $\partial_t |\psi_\alpha(t)\rangle = -i \sum_\beta \mathcal{M}_{\beta\alpha}(t) |\psi_\beta(t)\rangle$, and $|\mathcal{M}_{\alpha\beta}(t)| \lesssim \lambda \delta \varepsilon(t)$.
[81] The freedom in choosing a $\mathbf{k}$-dependent gauge for $|\psi_\alpha\rangle$ does not affect our discussion, since diagonal elements of $\mathcal{M}$ do not enter in our derivation.

Appendix A: Derivation of Eq. (11)

In this Appendix, we derive the expression for the time-averaged energy conversion rate from a single electron in band α, $\bar{P}_\alpha(\mathbf{k})$, that we quote in Eq. (11) in the main text.

To recapitulate, the equation we aim to derive [Eq. (11)] reads

$$\bar{P}_\alpha(\mathbf{k}) = f_1 f_2 \frac{e^2}{4\pi^2\hbar} \int_0^{2\pi} \mathrm{d}\phi_1 \mathrm{d}\phi_2 \, (\partial_{\phi_1} \boldsymbol{\alpha} \times \partial_{\phi_2} \boldsymbol{\alpha}) \cdot \boldsymbol{\Omega}_\alpha(\mathbf{k} + e\boldsymbol{\alpha}/\hbar). \tag{A1}$$

where we suppressed the (ϕ_1, ϕ_2)-dependence of the integrand. The quantities above are defined in the main text. For brevity, we will use the shorthand notation $\phi = (\phi_1, \phi_2)$ and $\boldsymbol{\Omega}_\alpha(\mathbf{k}, \phi) \equiv \boldsymbol{\Omega}_\alpha(\mathbf{k} + e\boldsymbol{\alpha}/\hbar)$ in the following.

We derive Eq. (A1) starting from Eq.(10) in the main text:

$$\bar{P}_\alpha(\mathbf{k}) = \frac{-e}{4\pi^2} \int_0^{2\pi} \mathrm{d}^2\phi \, \boldsymbol{\epsilon}_1(\phi) \cdot \mathbf{v}_\alpha(\mathbf{k}; \phi). \tag{A2}$$

Here $\boldsymbol{\epsilon}_i(\phi)$ denotes the electric field of mode i as a function of ϕ [74], while $\mathbf{v}_\alpha(\mathbf{k}; \phi)$ denotes the wavepacket velocity in band α as a function of ϕ, and is given by

$$\mathbf{v}_\alpha(\mathbf{k}; \phi) = \frac{1}{\hbar} \nabla \varepsilon_\alpha(\mathbf{k}, \phi) - \frac{e}{\hbar} \boldsymbol{\epsilon}(\phi) \times \boldsymbol{\Omega}_\alpha(\mathbf{k}, \phi) \tag{A3}$$

with $\boldsymbol{\epsilon}(\phi) = \boldsymbol{\epsilon}_1(\phi) + \boldsymbol{\epsilon}_2(\phi)$, $\varepsilon_\alpha(\mathbf{k}, \phi) \equiv \varepsilon_\alpha(\mathbf{k} + e\boldsymbol{\alpha}(\phi)/\hbar)$ and $\varepsilon_\alpha(\mathbf{k})$ denoting the energy of band α.

First, we consider the contribution to $\bar{P}_\alpha(\mathbf{k})$ from the group velocity component of $\mathbf{v}_\alpha$:

$$\bar{P}_{\alpha;\mathrm{gv}}(\mathbf{k}) \equiv \frac{-e}{4\pi^2\hbar} \int_0^{2\pi} \mathrm{d}^2\phi \, \boldsymbol{\epsilon}_1(\phi) \cdot \nabla \varepsilon_\alpha(\mathbf{k}, \phi) \tag{A4}$$

Using $\boldsymbol{\epsilon}_i(\phi) = \omega_i \partial_{\phi_i} \boldsymbol{\alpha}(\phi)$ along with the chain rule, one can verify that

$$-e\boldsymbol{\epsilon}_1(\phi) \cdot \nabla \varepsilon_\alpha(\mathbf{k}, \phi) = \hbar\omega_1 \partial_{\phi_1} \varepsilon_\alpha(\mathbf{k}, \phi). \tag{A5}$$

Since $\varepsilon_\alpha(\mathbf{k}, \phi)$ is 2π-periodic in ϕ_1, we conclude $\bar{P}_{\alpha;\mathrm{gv}}(\mathbf{k}) = 0$, implying that

$$\bar{P}_\alpha(\mathbf{k}) = \frac{-e^2}{4\pi^2\hbar} \int_0^{2\pi} \mathrm{d}^2\phi \, \boldsymbol{\epsilon}_1(\phi) \cdot [\boldsymbol{\epsilon}(\phi) \times \boldsymbol{\Omega}_\alpha(\mathbf{k}, \phi)] \tag{A6}$$

To evaluate Eq. (A6), we use that $\boldsymbol{\epsilon}(\phi) = \boldsymbol{\epsilon}_1(\phi) + \boldsymbol{\epsilon}_2(\phi)$, along with $\mathbf{a} \cdot (\mathbf{b} \times \mathbf{c}) = \mathbf{c} \cdot (\mathbf{a} \times \mathbf{b})$, we obtain

$$\bar{P}_\alpha(\mathbf{k}) = \frac{-e^2}{4\pi^2\hbar} \int_0^{2\pi} \mathrm{d}^2\phi \, [\boldsymbol{\epsilon}_1(\phi) \times \boldsymbol{\epsilon}_2(\phi)] \cdot \boldsymbol{\Omega}_\alpha(\mathbf{k}, \phi) \cdot \tag{A7}$$

Using $\boldsymbol{\epsilon}_i = \omega_i \partial_{\phi_i} \boldsymbol{\alpha}$ and $\omega_i = 2\pi f_i$, we identify

$$\boldsymbol{\epsilon}_1(\phi) \times \boldsymbol{\epsilon}_2(\phi) = \omega_1\omega_2 \partial_{\phi_1} \boldsymbol{\alpha} \times \partial_{\phi_2} \boldsymbol{\alpha}. \tag{A8}$$

Inserting this in the above establishes Eq. (A1).

Appendix B: Solution of master equation

Here solve the master equation in Eq. (24), and use the solution to obtain the expression for the current density in Eq. (21).

The Appendix is structured as follows: We provide a summary of the results in Sec. B 1. In Sec. B 2 we derive the steady state solution to the master equation. We demonstrate our solution for the Boltzmann-form dissipator in Sec. B 3. Using our steady state solution, in Sec. B 4 we obtain the current density, while Sec. B 5 contains derivations of auxiliary results which enter in our calculation.

1. Summary of solution

Our goal is to obtain the steady-state of the master equation

$$\partial_t \hat{\rho}(\mathbf{k}, t) = -\frac{i}{\hbar} [\hat{H}(\mathbf{k}, t), \hat{\rho}(\mathbf{k}, t)] + \mathcal{D}(\mathbf{k}, t) \circ \hat{\rho}(\mathbf{k}, t). \tag{B1}$$

Here $\hat{\rho}(\mathbf{k}, t)$ and $\hat{H}(\mathbf{k}, t)$ denote the momentum-resolved density matrix and Hamiltonian in the second-quantized Bloch space of the system, $\mathcal{H}_2$, while $\mathcal{D}(\mathbf{k}, t)$ is Lindblad-form superoperator. $\hat{H}(\mathbf{k}, t)$ is given by $\sum_{ij} \langle i|H(\mathbf{k}, t)|j\rangle \hat{c}_i^\dagger \hat{c}_j$, where $H(\mathbf{k}, t)$ denotes the ordinary (first-quantized) Bloch Hamiltonian of the system, and $\hat{c}_i$ annihilates a fermion in orbital α; see Sec. III for further details of the notation.

We solve Eq. (B1) in the limit where dynamics are adiabatic, and the characteristic relaxation rate $\Gamma =$

$\|\mathcal{D}(\mathbf{k},t)\|$ is slower than the characteristic angular driving frequency, Ω. This limit is summarized through the following conditions:

$$\Gamma \ll \Omega, \quad \hbar\Omega \ll \delta\varepsilon(\mathbf{k},t), \quad \hbar\partial_t H(\mathbf{k},t) \ll \delta\varepsilon^2(\mathbf{k},t), \tag{B2}$$

where $\delta\varepsilon(\mathbf{k},t)$ denotes the (smallest) spectral gap of $H(\mathbf{k},t)$. The second and third inequality are independent conditions that are both needed to ensure adiabatic dynamics.

To quantify the extent to which the system satisfies the conditions in Eq. (B2), we use the dimensionless parameter

$$\lambda(\mathbf{k}) \equiv \max_t \left(\frac{\Gamma}{\Omega}, \frac{\hbar\Omega}{\delta\varepsilon(\mathbf{k},t)}, \frac{\hbar\partial_t H(\mathbf{k},t)}{\delta\varepsilon^2(\mathbf{k},t)} \right). \tag{B3}$$

The system satisfies the conditions in Eq. (B2) for wavevectors $\mathbf{k}$ where $\lambda(\mathbf{k}) \ll 1$. In Sec. B 2, we derive the steady-state solution of Eq. (B1) up to a correction of order $\lambda^2(\mathbf{k})$.

From our steady-state solution we obtain the current density using

$$\mathbf{j}(t) = -\frac{e}{\hbar} \int \frac{\mathrm{d}^3\mathbf{k}}{(2\pi)^3} \mathrm{Tr}[\nabla \hat{H}(\mathbf{k},t)\hat{\rho}(\mathbf{k},t)]. \tag{B4}$$

The relevant property of the steady state in this computation are the band occupancies of the instantaneous Hamiltonian:

$$\rho_\alpha(\mathbf{k},t) \equiv \mathrm{Tr}[\hat{\rho}(\mathbf{k},t)\hat{\psi}^\dagger_\alpha(\mathbf{k},t)\hat{\psi}_\alpha(\mathbf{k},t)], \tag{B5}$$

where $\hat{\psi}_\alpha(\mathbf{k},t) = \sum_i \langle i|\psi_\alpha(\mathbf{k},t)\rangle \hat{c}_i$, denotes the αth eigenmode of $\hat{H}(\mathbf{k},t)$, with $|\psi_\alpha(\mathbf{k},t)\rangle$ denoting the αth eigenstate of $H(\mathbf{k},t)$ with associated energy $\varepsilon_\alpha(\mathbf{k},t)$. In Sec. B 4, we show that the integrand in Eq. (B4) can be expressed in terms of ρ_α as follows:

$$\frac{1}{\hbar}\mathrm{Tr}[\nabla \hat{H}(\mathbf{k},t)\hat{\rho}(\mathbf{k},t)] = \sum_\alpha \rho_\alpha(\mathbf{k},t)\dot{\mathbf{r}}_\alpha(\mathbf{k},t) + \mathcal{O}\left(\lambda^2(\mathbf{k})v_\mathrm{F}\right), \tag{B6}$$

where $\dot{\mathbf{r}}_\alpha(\mathbf{k},t) \equiv \nabla\varepsilon_\alpha(\mathbf{k},t) - \frac{e}{\hbar}\mathbf{E}(t)\times\mathbf{\Omega}_\alpha(\mathbf{k},t)$ denotes the group velocity in band α, and and v_F denotes the characteristic magnitude of $\|\nabla H(\mathbf{k},t)\|/\hbar$. This constitutes the main result of this appendix.

We provide a prescription for computing $\rho_\alpha(\mathbf{k},t)$ in Sec. B 2 d, and demonstrate the computation for the case of a Boltzmann-type dissipator in Sec. B 3.

a. *Decomposition of current density*

We now show how Eq. (B6) allows us to decompose the current density as

$$\mathbf{j}(t) = \mathbf{j}_0(t) + \delta\mathbf{j}(t), \tag{B7}$$

where

$$\mathbf{j}_0(t) = -e\int \frac{\mathrm{d}^3\mathbf{k}}{(2\pi)^3} \sum_\alpha \bar{\rho}_\alpha(\mathbf{k})\dot{\mathbf{r}}_\alpha(\mathbf{k},t), \tag{B8}$$

with $\bar{\rho}_\alpha(\mathbf{k})$ denoting the time-average of $\bar{\rho}_\alpha(\mathbf{k},t)$, and $\delta\mathbf{j}(t)$ denotes a dissipative component of the current density, which we define below, and which is small in the limit $\lambda(\mathbf{k}) \ll 1$. This result was quoted in Eq. (21) of the main text.

As our first step, we find that $\rho_\alpha(\mathbf{k},t)$ is nearly stationary in the limit $\Gamma \ll \Omega$:

$$\rho_\alpha(\mathbf{k},t) = \bar{\rho}_\alpha(\mathbf{k}) + \mathcal{O}(\Gamma/\Omega) + \mathcal{O}(\lambda^2(\mathbf{k})). \tag{B9}$$

This result is established in Sec. B 5 a. Note that $\Gamma/\Omega \leq \lambda(\mathbf{k})$, such that $v_\mathrm{mr}(\mathbf{k},t) \lesssim \lambda(\mathbf{k})v_\mathrm{F}$. However, we expressed this $\mathcal{O}(\lambda)$ correction as above to make it explicitly clear that it is controlled by Γ/Ω.

Next, we use that the two components of the group velocity satisfy

$$\frac{1}{\hbar}\nabla\varepsilon_\alpha(\mathbf{k},t) \lesssim v_\mathrm{F}, \quad \frac{e}{\hbar}|\mathbf{E}(t)\times\mathbf{\Omega}_\alpha(\mathbf{k},t)| \lesssim \lambda(\mathbf{k})v_\mathrm{F}. \tag{B10}$$

These results are established in Sec. B 5 b.

The above two results motivate us to decompose Eq. (B6) as

$$\frac{1}{\hbar}\mathrm{Tr}[\nabla \hat{H}(\mathbf{k},t)\hat{\rho}(\mathbf{k},t)] = \mathbf{v}_0(\mathbf{k},t) + \mathbf{v}_\mathrm{mr}(\mathbf{k},t) + \mathbf{v}_\mathrm{na}(\mathbf{k},t). \tag{B11}$$

where

$$\mathbf{v}_0(\mathbf{k},t) \equiv \sum_\alpha \bar{\rho}_\alpha(\mathbf{k})\dot{\mathbf{r}}_\alpha(\mathbf{k},t) \tag{B12}$$

$$\mathbf{v}_\mathrm{mr}(\mathbf{k},t) \equiv \frac{1}{\hbar}\sum_\alpha (\rho_\alpha(\mathbf{k},t) - \bar{\rho}_\alpha(\mathbf{k}))\nabla\varepsilon_\alpha(\mathbf{k},t)$$

$$\mathbf{v}_\mathrm{na}(\mathbf{k},t) \equiv \frac{1}{\hbar}\mathrm{Tr}[\nabla \hat{H}(\mathbf{k},t)\hat{\rho}(\mathbf{k},t)] - \mathbf{v}_0(\mathbf{k},t) - \mathbf{v}_\mathrm{mr}(\mathbf{k},t)$$

Due to Eqs. (B9) and (B10), the latter two components in particular satisfy

$$\mathbf{v}_\mathrm{mr}(\mathbf{k},t) \lesssim \mathcal{O}(v_\mathrm{F}\Gamma/\Omega) + \mathcal{O}(\lambda^2(\mathbf{k})v_\mathrm{F}), \tag{B13}$$

$$\mathbf{v}_\mathrm{na}(\mathbf{k},t) \lesssim \mathcal{O}(\lambda^2(\mathbf{k})v_\mathrm{F}). \tag{B14}$$

The decomposition above allows us to express the current density as

$$\mathbf{j}(t) = \mathbf{j}_0(t) + \mathbf{j}_\mathrm{mr}(t) + \mathbf{j}_\mathrm{na}(t) \tag{B15}$$

where

$$\mathbf{j}_\mathrm{mr}(t) = -\frac{e}{\hbar}\int \frac{\mathrm{d}^3\mathbf{k}}{(2\pi)^3}\mathbf{v}_\mathrm{mr}(\mathbf{k},t), \tag{B16}$$

$$\mathbf{j}_\mathrm{na}(t) = -\frac{e}{\hbar}\int \frac{\mathrm{d}^3\mathbf{k}}{(2\pi)^3}\mathbf{v}_\mathrm{na}(\mathbf{k},t). \tag{B17}$$

We identify $\delta\mathbf{j}(t) = \mathbf{j}_\mathrm{na}(t) + \mathbf{j}_\mathrm{mr}(t)$. Evidently, $\mathbf{j}_0$ dominates in the limit of adiabatic driving and coherent dynamics, where $\lambda(\mathbf{k}) \ll 1$.

$\mathbf{j}_\mathrm{mr}$ is the current density correction due to relaxation-induced fluctuations in the band-occupancy, while $\mathbf{j}_\mathrm{na}$ as the correction due to the finite driving frequency and relaxation rate (relative to the band gap). Note that $\mathbf{j}_\mathrm{na}(t)$

is only significant for $\mathbf{k}$-points where dynamics are non-adiabatic, while $\mathbf{j}_{\rm mr}(t)$ can be nonzero for all $\mathbf{k}$-points where the electron density fluctuates. For this reason, we heuristically identify $\mathbf{j}_{\rm mr}$ and $\mathbf{j}_{\rm na}$ as the components of $\delta\mathbf{j}(t)$ that arise due to momentum relaxation and non-adiabatic heating, respectively.

2. Derivation of steady state

In this subsection we derive the steady state solution of Eq. (B1).

We first show that such a steady state exists. Given an initial condition specified at some time t_0, the solution of Eq. (B1) can formally be written as

$$\hat{\rho}(\mathbf{k},t) = \mathcal{T} e^{\int_{t_0}^{t} ds \mathcal{L}(s)} \circ \hat{\rho}(\mathbf{k},t_0). \tag{B18}$$

where $\mathcal{T}$ denotes time-ordering, and $\mathcal{L}(\mathbf{k},t)$ denotes the Liouvillian generating the time-evolution: $\mathcal{L}(\mathbf{k},t)\circ\hat{\mathcal{O}} = -(i/\hbar)[\hat{H}(\mathbf{k},t),\hat{\mathcal{O}}] + \mathcal{D}(\mathbf{k},t)\circ\hat{\mathcal{O}}$.

Due to its Lindblad form, $\mathcal{L}(\mathbf{k},t)$ is negative semidefinite. Except in cases of fine-tuning or in the presence of conserved integrals of motion (which we do not consider here), all eigenvalues of $\mathcal{L}(\mathbf{k},t)$ except for one are negative; the last eigenvalue takes value 0. The left eigenvector corresponding to this unique zero-eigenvalue is the identity operator, $\hat{I}$ [75] It follows that $\lim_{t_0\to-\infty} \mathcal{T} e^{\int_{t_0}^{t} ds \mathcal{L}(\mathbf{k},s)}$ has a single left eigenvector with eigenvalue 1 (namely $\hat{I}$), while all other eigenvalues vanish. Letting $\hat{\rho}(\mathbf{k},t;t_0)$ denote the corresponding right eigenvector, we hence have

$$\lim_{t_0\to-\infty} \mathcal{T} e^{\int_{t_0}^{t} ds \mathcal{L}(\mathbf{k},s)} \circ \hat{M} = \hat{\rho}_0(\mathbf{k},t;t_0)\mathrm{Tr}[\hat{M}] \tag{B19}$$

$\mathcal{L}(\mathbf{k},t)$ preserves the trace and positivity of any operator and we may choose $\hat{M}$ positive-definite. Hence $\hat{\rho}_0(\mathbf{k},t;t_0)$ must be positive-definite and have unit trace. In other words, $\hat{\rho}_0(\mathbf{k},t;t_0)$ corresponds to a physical density matrix.

The semigroup property, $\mathcal{T} e^{\int_{t_0}^{t} ds \mathcal{L}(\mathbf{k},s)} \circ M = \mathcal{T} e^{\int_{t_1}^{t} ds \mathcal{L}(\mathbf{k},s)} \circ (\mathcal{T} e^{\int_{t_0}^{t_1} ds \mathcal{L}(\mathbf{k},s)} \circ M)$ implies that $\hat{\rho}_0(\mathbf{k},t;t_0)$ must be independent of t_0 in the limit $t_0 \to -\infty$. We thus simply refer to this operator as $\hat{\rho}_0(\mathbf{k},t)$. This operator defines the time-dependent steady state of the system. Our goal is to obtain this steady state.

Eq. (B19) implies we can obtain the steady state by evolving Eq. (B1) from any initial state with unit trace; for our purpose it is convenient to choose the initial state $\hat{\rho}(\mathbf{k},t_0) = \hat{I}/2^d$, where $\hat{I}$ denotes the identity operator. Our derivation proceeds as follows: we first identify a time-dependent unitary transformation (or "comoving frame transformation") that maps Eq. (B1) into a new master equation of the same form in which the eigenbasis of the Hamiltonian is constant up to a correction of order λ^2; this approach was e.g. also used in Ref. [76]. We then solve the master equation in this new frame using a rotating wave approximation, by exploiting that the spectral gap of the Hamiltonian is the largest energy scale of the system in the limit $\lambda(\mathbf{k}) \ll 1$ [77, 78].

In the following, we consider the dynamics of electrons with a fixed given wavevector, $\mathbf{k}$. For brevity, we suppress all quantities' dependence on $\mathbf{k}$, unless otherwise noted.

a. Rotating frame transformation

Here we map the master equation in Eq. (B1) into one where the Hamiltonian has an effectively time-independent eigenbasis. To this end, we sequentially apply two comoving frame transformations that each reduce the time-dependence of the Hamiltonian's eigenstates by a factor λ [76]. The first transformation, $\hat{Q}_1(t)$, maps $\hat{\psi}_\alpha(t)$ into the orbital annihilation operator $\hat{c}_\alpha$, for all α:

$$\hat{Q}_1^\dagger(t)\hat{\psi}_\alpha(t)\hat{Q}_1(t) = \hat{c}_\alpha \tag{B20}$$

As we show in Sec. B 5 c, the above is realized when

$$\hat{Q}_1(t) = \mathcal{T} e^{-i\int_0^t ds \sum_{\alpha\beta} \mathcal{M}_{\alpha\beta}(s)\hat{\psi}_\alpha^\dagger(s)\hat{\psi}_\beta(s)} \hat{V}_1, \tag{B21}$$

where

$$\mathcal{M}_{\alpha\beta}(t) = i\langle\psi_\alpha(t)|\partial_t\psi_\beta(t)\rangle \tag{B22}$$

and $\hat{V}_1 = \exp(\sum_{ij}\hat{c}_i^\dagger\hat{c}_j\log(M)_{ij})$, with $\log(M)$ denoting the logarithm of the matrix with entries $M_{ij} = \langle\psi_i(0)|j\rangle$. Since $\langle\psi_\alpha(t)|\partial_t\psi_\beta(t)\rangle = -\langle\partial_t\psi_\alpha(t)|\psi_\beta(t)\rangle$, $\mathcal{M}_{\alpha\beta}(t)$ is Hermitian. Without loss of generality, we choose to work in a gauge where $\langle\psi_\alpha|\partial_t\psi_\alpha\rangle = 0$, implying $\mathcal{M}_{\alpha\alpha}(t) = 0$.

We consider the evolution of the system in the rotating frame that results after applying $\hat{Q}_1(t)$. I.e., we consider the evolution of

$$\hat{\rho}_1(t) \equiv \hat{Q}_1^\dagger(t)\hat{\rho}(t)\hat{Q}_1(t). \tag{B23}$$

By taking the time-derivative of $\hat{\rho}_1(t)$ and exploiting $\partial_t\hat{Q}_1(t) = -i\sum_{\alpha\beta}\mathcal{M}_{\alpha\beta}(t)\hat{\psi}_\alpha^\dagger(t)\hat{\psi}_\beta(t)\hat{Q}_1(t)$, we find that

$$\partial_t\hat{\rho}_1(t) = -\frac{i}{\hbar}[\hat{H}_1(t),\hat{\rho}_1(t)] + \mathcal{D}_1(t)\circ\hat{\rho}_1(t). \tag{B24}$$

where

$$\hat{H}_1(t) = \sum_\alpha \varepsilon_\alpha(t)\hat{c}_\alpha^\dagger\hat{c}_\alpha - \sum_{\alpha\beta}\mathcal{M}_{\alpha\beta}(t)\hat{c}_\alpha^\dagger\hat{c}_\beta. \tag{B25}$$

and

$$\mathcal{D}_1\circ\hat{\mathcal{O}} = Q_1^\dagger\Big[\mathcal{D}\circ(\hat{Q}_1\hat{\mathcal{O}}\hat{Q}_1^\dagger)\Big]\hat{Q}_1, \tag{B26}$$

with time-dependence suppressed for brevity. Note that $\mathcal{D}_1(t)$ is in the Lindblad-form.

Eq. (B24) is of the same form as the original master equation we considered, Eq. (B1). However, the eigenmodes of the new Hamiltonian $\hat{H}_1(t)$, $\hat{\psi}^1_\alpha(t)$ are nearly stationary. To see this, note that, for $\alpha \neq \beta$,

$$\mathcal{M}_{\alpha\beta}(t) = -i\frac{\langle\psi_\alpha(t)|\partial_t H(t)|\psi_\beta(t)\rangle}{2(\varepsilon_\alpha(t)-\varepsilon_\beta(t))} \tag{B27}$$

implying

$$|\mathcal{M}_{\alpha\beta}(t)| \lesssim \lambda\delta\varepsilon(t). \tag{B28}$$

Thus, in the adiabatic limit, $\lambda \ll 1$, $\hat{\psi}^1_\alpha(t)$ can be computed using canonical perturbation theory with respect to the term $\sum_{\alpha\beta}\mathcal{M}_{\alpha\beta}(t)\hat{c}^\dagger_\alpha\hat{c}_\beta$ in Eq. (B25). The nth term in this expansion will be of order λ^n, and first order expansion thus yields

$$\hat{\psi}^1_\alpha(t) = \hat{c}_\alpha - \sum_{\beta\neq\alpha}\frac{\mathcal{M}_{\alpha\beta}(t)}{\varepsilon_\alpha(t)-\varepsilon_\beta(t)}\hat{c}_\beta + \mathcal{O}\left(\lambda^2\right), \tag{B29}$$

The expression above gives $\hat{\psi}^1_\alpha(t)$ up to an overall (time-dependent) phase factor which we are free to choose due to gauge symmetry. Similar perturbative arguments show that the associated energies of $\hat{H}_1(t)$ are given by $\varepsilon^1_\alpha(t) = \varepsilon_\alpha(t) + \mathcal{O}(\lambda^2\delta\varepsilon)$, since we chose a gauge for $|\psi_\alpha(t)\rangle$ where $\mathcal{M}_{\alpha\alpha}(t) = 0$. Evidently, the αth eigenmode of the transformed Hamiltonian, $\hat{\psi}^1_\alpha(t)$, is given by $\hat{c}_\alpha$, up to a time-dependent correction of order λ. Hence the eigenmodes of $\hat{H}_1(t)$ are nearly stationary in the limit $\lambda \ll 1$.

We now apply the above procedure one more time. We first apply a comoving frame transformation $\hat{Q}_2(t)$ to $\hat{H}_1(t)$ which transforms each eigenmodes $\hat{\psi}^1_\alpha(t)$ into the orbital annihilation operator $\hat{c}_\alpha$:

$$\hat{Q}^\dagger_2(t)\hat{\psi}^1_\alpha(t)\hat{Q}_2(t) = \hat{c}_\alpha. \tag{B30}$$

Since $\hat{\psi}^1_\alpha(t) = \hat{c}_\alpha + \mathcal{O}(\lambda)$, $\hat{Q}_2(t) = 1 + \mathcal{O}(\lambda)$. We can find $\hat{Q}_2(t)$ exactly using the same procedure we used to obtain $\hat{Q}_1(t)$. Following this procedure, we find the density matrix in this frame, $\hat{Q}_2(t)\hat{\rho}_1(t)\hat{Q}^\dagger_2(t)$ evolves according to the master equation

$$\partial_t\hat{\rho}_2(t) = -\frac{i}{\hbar}[\hat{H}_2(t),\hat{\rho}(t)] - \mathcal{D}_2(t)\circ\hat{\rho}_0(t). \tag{B31}$$

where $\mathcal{D}_2\circ\hat{\mathcal{O}} = \hat{Q}_2\big[\mathcal{D}_1\circ(\hat{Q}_2\hat{\mathcal{O}}\hat{Q}^\dagger_2\big]\hat{Q}_2$ (with time-dependence suppressed for brevity), and

$$\hat{H}_2(t) = \sum_\alpha\varepsilon^1_\alpha(t)\hat{c}^\dagger_\alpha\hat{c}_\alpha + \sum_{\alpha\beta}\mathcal{M}^1_{\alpha\beta}(t)\hat{c}^\dagger_\alpha\hat{c}_\beta. \tag{B32}$$

Here $\mathcal{M}^1_{\alpha\beta}(t) \equiv i\langle\psi^1_\alpha(t)|\partial_t\psi^1_\beta(t)\rangle$, with $|\psi^1_\alpha(t)\rangle = \hat{\psi}^{1\dagger}_\alpha(t)|0\rangle$ denoting the single-particle eigenstate of $\hat{H}_1(t)$ with associated energy $\varepsilon^1_\alpha(t)$.

We now seek to bound $\mathcal{M}^1_{\alpha\beta}$. To this end, we use that $\partial_t(\varepsilon_\alpha(t)-\varepsilon_\beta(t))^{-1} \lesssim \lambda$ [79], $\partial_t|\psi_\alpha(t)\rangle \lesssim \lambda\delta\varepsilon(t)$ [80], and $\partial^2_t H(t) \sim \Omega\partial_t H(t) \leq \lambda^2\delta\varepsilon^2(t)$. Combining these results with Eq. (B27), we conclude $\partial_t\mathcal{M}_{\alpha\beta}(t) \sim \lambda^2\delta\varepsilon(t)$. Using Eq. (B29), $\partial_t(\varepsilon_\alpha(t)-\varepsilon_\beta(t))^{-1} \lesssim \lambda$, and the definition of $\mathcal{M}^1_{\alpha\beta}(t)$, we hence obtain

$$\mathcal{M}^1_{\alpha\beta}(t) \sim \lambda^2\delta\varepsilon(t) \tag{B33}$$

In principle we could iterate the comoving frame transformation procedure further to obtain increasingly accurate master equations for $\hat{\rho}(\mathbf{k},t)$ [76]. However, since we are just interested in obtaining $\hat{\rho}(\mathbf{k},t)$ to corrections of order λ^2, this second step is enough for our purpose.

b. Rotating wave approximation

We now solve Eq. (B31) with a rotating wave approximation. To this end, we first apply a *final* unitary transformation to Eq. (B31) which is generated by diagonal part of $\hat{H}_2(t)$:

$$\hat{V}(t) = \exp\left[-i\int_0^t \mathrm{d}t\sum_\alpha\varepsilon^1_\alpha(t)\hat{c}^\dagger_\alpha\hat{c}_\alpha\right]. \tag{B34}$$

The density matrix in this frame, $\tilde{\rho}(t) = \hat{V}^\dagger(t)\hat{\rho}_2(t)\hat{V}(t)$, evolves according to the master equation

$$\partial_t\tilde{\rho} = \hat{V}^\dagger\Big(\mathcal{L}_2\circ[\hat{V}\tilde{\rho}\hat{V}^\dagger]\Big)\hat{V}. \tag{B35}$$

where

$$\mathcal{L}_2\circ\hat{\mathcal{O}} = -\frac{i}{\hbar}[\sum_{\alpha\beta}\mathcal{M}^1_{\alpha\beta}\hat{c}^\dagger_\alpha\hat{c}_\beta,\hat{\mathcal{O}}] + \mathcal{D}_2\circ\hat{\mathcal{O}}. \tag{B36}$$

Here we suppressed time-dependence for brevity.

We consider the matrix elements of $\tilde{\rho}(t)$ in the basis of states corresponding to the 2^d unique configurations of electrons in the orbitals in the system, $\{|\boldsymbol{n}\rangle\}$,

$$p_{\boldsymbol{mn}}(t) \equiv \langle\boldsymbol{m}|\hat{\rho}(t)|\boldsymbol{n}\rangle. \tag{B37}$$

Here, $\boldsymbol{n} = (n_1,\dots n_d)$ with $n_i = 0,1$ for each i and $\hat{c}^\dagger_i\hat{c}_i|\boldsymbol{n}\rangle = n_i|\boldsymbol{n}\rangle$. I.e., $|\boldsymbol{n}\rangle$ denotes the state in $\mathcal{H}_2$ with n_i Fermions in orbital i. In this basis t orbital basis of $\mathcal{H}_2$. Here and below, we use bold italic symbols to indicate configurations of orbital occupancies, as above.

According to Eq. (B35), $p_{\boldsymbol{mn}}(t)$ evolves according to the coupled differential equation

$$\partial_t p_{\boldsymbol{nm}}(t) = \sum_{\boldsymbol{kl}}^N R^{\boldsymbol{kl}}_{\boldsymbol{nm}}(t)p_{\boldsymbol{kl}}(t) \tag{B38}$$

where

$$R^{\boldsymbol{kl}}_{\boldsymbol{nm}}(t) \equiv \langle\boldsymbol{n}|\mathcal{L}_2(t)\circ(|\boldsymbol{k}\rangle\langle\boldsymbol{l}|)|\boldsymbol{m}\rangle e^{i\int_0^t ds\sum_i\varepsilon^2_i(t)(n_i-m_i+k_i-l_i)}. \tag{B39}$$

Note that $\mathcal{L}_2(t)$ is of order $\lambda^2\delta\varepsilon(t)$. This follows since $\mathcal{M}^1_{\alpha\beta} \sim \lambda^2\delta\varepsilon(t)$ and $\|\mathcal{D}_2\| = \|\mathcal{D}\| \leq \Gamma$, while $\Gamma \leq \lambda^2\delta\varepsilon(t)$.

At the same time, we expect $\langle \boldsymbol{n}|\tilde{\mathcal{L}}_2(t)\circ(|\boldsymbol{k}\rangle\langle\boldsymbol{l}|)|\boldsymbol{m}\rangle$ oscillates with characteristic frequency Ω. In the limit $\lambda \ll 1$, $R^{\boldsymbol{kl}}_{\boldsymbol{nm}}(t)$ hence oscillates rapidly relative to its characteristic magnitude for choices of $\boldsymbol{n},\boldsymbol{m},\boldsymbol{k},\boldsymbol{l}$ where $n_i - m_i \neq k_i - l_i$ for one or more choices i. This allows us to make a rotating wave approximation, where we only keep the terms in Eq. (B39) where $n_i - m_i = k_i - l_i$ for all i. We expect this approximation yields the correct steady state up to a correction of order $\|\mathcal{L}_2\|/\delta\varepsilon \sim \lambda^2$ [77].

After the rotating wave approximation above, Eq. (B39) in particular only couples diagonal matrix elements of $\tilde{\rho}$ with other diagonal elements:

$$\partial_t p_{\boldsymbol{nn}}(t) = -\sum_{\boldsymbol{m}} R^{\boldsymbol{mm}}_{\boldsymbol{nn}}(t) p_{\boldsymbol{mm}}(t). \tag{B40}$$

Since we chose the initial condition $\hat{\rho}(t_0) = \hat{I}/2^d$, implying $p_{\boldsymbol{nm}}(t_0) = 1/2^d \delta_{\boldsymbol{nm}}$, we hence conclude

$$\tilde{\rho}(t) = \sum_{\boldsymbol{n}} f_{\boldsymbol{n}}(t)|\boldsymbol{n}\rangle\langle\boldsymbol{n}| + \mathcal{O}(\lambda^2). \tag{B41}$$

where $f_{\boldsymbol{n}}(t)$ denotes the steady state of

$$\partial_t f_{\boldsymbol{n}}(t) = -\sum_{k} R^{\boldsymbol{mm}}_{\boldsymbol{nn}}(t) f_{\boldsymbol{m}}(t) \tag{B42}$$

and is normalized such that $\sum_{\boldsymbol{n}} f_{\boldsymbol{n}}(t) = 1$. Evidently, $\tilde{\rho}(t)$ is diagonal in the orbital eigenbasis up to a correction of order λ^2, while the off-diagonal elements decohere (this is a general feature for open quantum systems where relaxation is slow compared to the level spacing of the system [77]).

We obtain the steady state in the lab frame, $\hat{\rho}(t)$ by reverting the net unitary transformation that we applied to obtain $\tilde{\rho}$,

$$\hat{U}(t) = \hat{V}(t)\hat{Q}_2(t)\hat{Q}_1(t). \tag{B43}$$

Thus we conclude

$$\hat{\rho}(t) = \sum_{\boldsymbol{n}} f_{\boldsymbol{n}}(t)\hat{U}^\dagger(t)|\boldsymbol{n}\rangle\langle\boldsymbol{n}|\hat{U}(t) + \mathcal{O}(\lambda^2) \tag{B44}$$

Here $f_{\boldsymbol{n}}(t)$ is computed from Eq. (B42).

c. *Direct method for computing $R^{\boldsymbol{mm}}_{\boldsymbol{nn}}$*

The matrix elements $R^{\boldsymbol{mm}}_{\boldsymbol{nn}}$, which determine the steady state through the coefficients $f_{\mathbf{n}}(t)$, can in principle be obtained from the definition in Eq. (B39). However, we can obtain them directly from the eigenstates of the instantaneous Hamiltonian $\hat{H}(t)$ and the lab frame dissipator $\mathcal{D}(t)$ without having to go through the procedure we described in Sec. B 2 a.

First note that $\mathcal{M}^1_{\alpha\alpha} = 0$, implying

$$R^{\boldsymbol{mm}}_{\boldsymbol{nn}}(t) = \mathrm{Tr}\big[\mathcal{D}_2(t)\circ(|\boldsymbol{m}\rangle\langle\boldsymbol{m}|)|\boldsymbol{n}\rangle\langle\boldsymbol{n}|\big] \tag{B45}$$

Next, we recall that

$$\mathcal{D}_2\circ\hat{\mathcal{O}} = \hat{Q}_1^\dagger\hat{Q}_2^\dagger\big[\mathcal{D}\circ(\hat{Q}_2\hat{Q}_1\hat{\mathcal{O}}\hat{Q}_1^\dagger\hat{Q}_2^\dagger)\big]\hat{Q}_2\hat{Q}_1, \tag{B46}$$

where we suppressed t. We now use that $\hat{Q}_2 = 1 + \mathcal{O}(\lambda)$ and

$$\hat{Q}_1(t)|\boldsymbol{n}\rangle = |\Psi_{\boldsymbol{n}}(t)\rangle \tag{B47}$$

where $|\Psi_{\boldsymbol{n}}(t)\rangle$ is the eigenstate of $\hat{H}(t)$ satisfying

$$\hat{\psi}^\dagger_\alpha(t)\hat{\psi}_\alpha(t)|\Psi_{\boldsymbol{n}}(t)\rangle = n_\alpha|\Psi_{\boldsymbol{n}}(t)\rangle. \tag{B48}$$

Combining the above results and using $\mathcal{D}(t) \sim \Gamma$, we thus obtain

$$R^{\boldsymbol{mm}}_{\boldsymbol{nn}} = \mathrm{Tr}\big[\mathcal{D}\circ(|\Psi_{\boldsymbol{m}}\rangle\langle\Psi_{\boldsymbol{m}}|)|\Psi_{\boldsymbol{n}}\rangle\langle\Psi_{\boldsymbol{n}}|\big] + \mathcal{O}(\lambda\Gamma). \tag{B49}$$

where we suppressed the time-dependence of $|\Psi_{\boldsymbol{n}}(t)\rangle$, $\mathcal{D}(t)$ and $R^{\boldsymbol{mm}}_{\boldsymbol{nn}}(t)$. Since $R^{\boldsymbol{mm}}_{\boldsymbol{nn}}(t) \sim \Gamma$, we expect neglecting the correction above yields the correct value of $f_{\boldsymbol{n}}(t)$ state up to a correction of order λ.

d. *Calculation of band occupancies*

Now, we compute the instantaneous occupancy in band α in the system, $\rho_\alpha(\mathbf{k},t)$, which will play an important role for determining the current density.

We consider the one-body correlation matrix in the eigenmode basis,

$$g_{\alpha\beta}(\mathbf{k},t) \equiv \mathrm{Tr}[\hat{\psi}^\dagger_\alpha(\mathbf{k},t)\hat{\psi}_\beta(\mathbf{k},t)\hat{\rho}(\mathbf{k},t)]. \tag{B50}$$

The instantaneous occupancy of band α is given by the diagonal elements of this matrix, $\rho_\alpha(\mathbf{k},t) = g_{\alpha\alpha}(\mathbf{k},t)$. However, we will also keep track of the off-diagonal elements of $g_{\alpha\beta}(\mathbf{k},t)$, since these are used to compute the current density in the next subsection. In the remainder of this step of the derivation, $\mathbf{k}$ and t are fixed parameters, and we therefore suppress them for brevity.

Inserting the solution for $\hat{\rho}$ we obtained Eq. (B44), we find

$$g_{\alpha\beta} = \sum_{\boldsymbol{n}} f_{\boldsymbol{n}}\langle\boldsymbol{n}|\hat{U}\hat{\psi}^\dagger_\alpha\hat{\psi}_\beta\hat{U}^\dagger|\boldsymbol{n}\rangle + \mathcal{O}(\lambda^2), \tag{B51}$$

where $\hat{U} = \hat{V}\hat{Q}_2\hat{Q}_1$. Since $|\boldsymbol{n}\rangle$ is an eigenstate of $\hat{V}$, and $\hat{Q}_1^\dagger\hat{\psi}_\alpha\hat{Q}_1 = \hat{c}_\alpha$, we find

$$g_{\alpha\beta} = \sum_{\boldsymbol{n}} f_{\boldsymbol{n}}\langle\boldsymbol{n}|\hat{Q}_2\hat{c}^\dagger_\alpha\hat{c}_\beta\hat{Q}_2^\dagger|\boldsymbol{n}\rangle + \mathcal{O}(\lambda^2) \tag{B52}$$

Since $\hat{Q}_2$ is a product of exponentials of a quadratic operators, $\hat{Q}_2^\dagger\hat{c}_\alpha\hat{Q}_2$ must be a linear combination of the operators $\{\hat{c}_i\}$; i.e.,

$$\hat{Q}_2^\dagger\hat{c}_\alpha\hat{Q}_2 = \sum_i Q_{\alpha i}\hat{c}_i \tag{B53}$$

for some unitary matrix $Q_{\alpha i}$ which we obtain below. Using $\langle \boldsymbol{n}|\hat{c}_i^\dagger \hat{c}_j|\boldsymbol{n}\rangle = \delta_{ij} n_i$, we thus find

$$g_{\alpha\beta} = \sum_{\boldsymbol{n},i} f_{\boldsymbol{n}} n_i Q^*_{\alpha i} Q_{\beta i} + \mathcal{O}(\lambda^2), \tag{B54}$$

To compute $Q_{\alpha i}$, we use Eqs. (B29)-(B30) to obtain

$$\hat{Q}_2 \hat{c}_\alpha \hat{Q}_2^\dagger = \hat{c}_\alpha + \sum_{\beta\neq\alpha} \frac{\mathcal{M}_{\alpha\beta}}{\varepsilon_\alpha - \varepsilon_\beta} \hat{c}_\beta + \mathcal{O}(\lambda^2) \tag{B55}$$

Combining this with Eq. (B53), we conclude

$$Q_{\alpha\beta} = \delta_{\alpha\beta} + \frac{\mathcal{M}_{\alpha\beta}}{\varepsilon_\alpha - \varepsilon_\beta}(1-\delta_{\alpha\beta}) + \mathcal{O}(\lambda^2) \tag{B56}$$

Inserting this result into Eq. (B54), we obtain

$$g_{\alpha\beta} = \sum_{\boldsymbol{n}} f_{\boldsymbol{n}} \left(\delta_{\alpha\beta} n_\alpha + \mathcal{M}_{\beta\alpha}(1-\delta_{\alpha\beta}) \frac{n_\alpha - n_\beta}{\varepsilon_\alpha - \varepsilon_\beta} \right) + \mathcal{O}(\lambda^2) \tag{B57}$$

where we used that $\frac{\mathcal{M}_{\beta\alpha}}{\varepsilon_\alpha - \varepsilon_\beta} \sim \mathcal{O}(\lambda)$. Setting $\alpha = \beta$ and using $\rho_\alpha = g_{\alpha\alpha}$, we hence find

$$\rho_\alpha = \sum_{\boldsymbol{n}} f_{\boldsymbol{n}} n_\alpha + \mathcal{O}(\lambda^2). \tag{B58}$$

3. Explicit solution for Boltzmann-form dissipator

We finally demonstrate our solution above for the case where $\mathcal{D}(\mathbf{k},t)$ is given by the Boltzmann-type dissipator in Eq. (26), $\mathcal{D}(\mathbf{k},t)\circ\hat{\mathcal{O}} = -\frac{1}{\tau}[\hat{\mathcal{O}} - \hat{\rho}^{\rm eq}_\alpha(\mathbf{k},t)]$. Here $\rho^{\rm eq}_\alpha(\mathbf{k},t)$ denotes the equilibrium state of the instantaneous Hamiltonian $\hat{H}(\mathbf{k},t)$ with temperature $1/\beta$ and chemical potential μ. We treat $\mathbf{k}$ as a fixed parameter and suppress it below.

First, we obtain the coefficients $f_{\boldsymbol{n}}(t)$, which determine the band occupancies $\rho_\alpha(t)$. Recall that $f_{\boldsymbol{n}}$ are given as the steady-state solution to the the differential equation in Eq. (B42), $\partial_t f_{\boldsymbol{n}}(t) = \sum_{\boldsymbol{m}} R^{\boldsymbol{nm}}_{\boldsymbol{nn}}(t) f_{\boldsymbol{m}}(t)$. Using Eq. (B49) to find the coefficients $\{R^{\boldsymbol{mm}}_{\boldsymbol{nn}}(t)\}$, a straightforward computation yields

$$R^{\boldsymbol{mm}}_{\boldsymbol{nn}}(t) = -\frac{1}{\tau}\delta_{\boldsymbol{nm}} + \frac{1}{\tau}\mathrm{Tr}\big[\hat{\rho}_{\rm eq}(t)|\Psi_{\boldsymbol{n}}(t)\rangle\langle\Psi_{\boldsymbol{n}}(t)|\big] \tag{B59}$$

Thus

$$\partial_t f_{\boldsymbol{n}}(t) = -\frac{1}{\tau} f_{\boldsymbol{n}}(t) + \frac{1}{\tau}\mathrm{Tr}\big[\hat{\rho}_{\rm eq}(t)|\Psi_{\boldsymbol{n}}(t)\rangle\langle\Psi_{\boldsymbol{n}}(t)|\big] \tag{B60}$$

where we used $\sum_{\boldsymbol{m}} f_{\boldsymbol{m}}(t) = 1$. This first-order inhomogeneous differential equation has steady-state solution

$$f_{\boldsymbol{n}}(t) = \frac{1}{\tau}\int_0^t ds e^{-(t-s)/\tau}\mathrm{Tr}\big[\hat{\rho}_{\rm eq}(s)|\Psi_{\boldsymbol{n}}(s)\rangle\langle\Psi_{\boldsymbol{n}}(s)|\big] \tag{B61}$$

Next, we obtain the band occupancies, $\{\rho_\alpha(t)\}$, using

$$\rho_\alpha(t) = \sum_{\boldsymbol{n}} f_{\boldsymbol{n}}(t) n_\alpha \tag{B62}$$

Substituting in Eq. (B61) and identifying $\sum_{\boldsymbol{n}} |\Psi_{\boldsymbol{n}}(t)\rangle\langle\Psi_{\boldsymbol{n}}(t)| n_\alpha = \hat{\psi}^\dagger_\alpha(t)\hat{\psi}_\alpha(t)$, we obtain

$$\rho_\alpha(t) = \frac{1}{\tau}\int_0^t ds e^{-(t-s)/\tau}\mathrm{Tr}[\hat{\rho}_{\rm eq}(s)\hat{\psi}^\dagger_\alpha(s)\hat{\psi}_\alpha(s)] \tag{B63}$$

Next, we note that $\mathrm{Tr}[\hat{\psi}^\dagger_\alpha(s)\hat{\psi}_\alpha(s)\hat{\rho}_{\rm eq}(s)]$ gives occupation probability of the αth band of the Hamiltonian $\hat{H}(t)$ in equilibrium at temperature $1/\beta$ and chemical potential μ. We recognize this probability as $f_\beta(\varepsilon_\alpha(s)-\mu)$ where $f_\beta(\varepsilon)$ denotes the Fermi-Dirac distribution at temperature $1/\beta$. Thus

$$\rho_\alpha(t) = \frac{1}{\tau}\int_0^t ds e^{-(t-s)/\tau} f_\beta(\varepsilon_\alpha(s)-\mu). \tag{B64}$$

Note that $\rho_\alpha(t)$ converges to its time-average in the limit $\tau^{-1} \ll \Omega$, consistently with what we claimed in Eq. (B9).

We finally compute the time-average of $\rho_\alpha(t)$. A straightforward computation shows

$$\bar{\rho}_\alpha = \lim_{t\to\infty}\frac{1}{t}\int_0^s dt f_\beta(\varepsilon_\alpha(s)-\mu). \tag{B65}$$

which was what we quoted in Eq. (27) in the main text.

4. Derivation of current density

We finally obtain the expression for the current density in Eq. (B6), i.e., we seek to show that

$$\frac{1}{\hbar}\mathrm{Tr}[\nabla\hat{H}\hat{\rho}] = \sum_\alpha \rho_\alpha \dot{\mathbf{r}}_\alpha + \mathcal{O}\left(\lambda^2 v_{\rm F}\right), \tag{B66}$$

where $\dot{\mathbf{r}}_\alpha = \frac{1}{\hbar}\nabla\varepsilon_\alpha - \frac{e}{\hbar}\mathbf{E}\times\boldsymbol{\Omega}_\alpha$. Here and below, we take both $\mathbf{k}$ and t to be implicit parameters.

As our first step, we combine $\mathrm{Tr}[\hat{\rho}\nabla\hat{H}] = \sum_{ij}\langle i|\nabla H|j\rangle\mathrm{Tr}[\hat{\rho}\hat{c}_i^\dagger\hat{c}_j]$. with $\hat{c}_i^\dagger = \sum_\alpha\langle\psi_\alpha|i\rangle\hat{\psi}^\dagger_\alpha$ to write

$$\mathrm{Tr}[\hat{\rho}\nabla\hat{H}] = \sum_{\alpha\beta}\langle\psi_\alpha|\nabla H|\psi_\beta\rangle g_{\alpha\beta}, \tag{B67}$$

where $g_{\alpha\beta} \equiv \mathrm{Tr}[\hat{\psi}^\dagger_\alpha\hat{\psi}_\beta]$ and is computed in Sec. B 2 d. Combining Eqs. (B57)-(B58) we can express $g_{\alpha\beta}$ in terms of the band occupancies ρ_α:

$$g_{\alpha\beta} = \delta_{\alpha\beta}\rho_\alpha + \mathcal{M}_{\beta\alpha}(1-\delta_{\alpha\beta})\frac{\rho_\alpha - \rho_\beta}{\varepsilon_\alpha - \varepsilon_\beta} + \mathcal{O}(\lambda^2) \tag{B68}$$

Next, we use the spectral decomposition $H = \sum_\alpha |\psi_\alpha\rangle\langle\psi_\alpha|\varepsilon_\alpha$ to find

$$\langle\psi_\alpha|\nabla H|\psi_\beta\rangle = \delta_{\alpha\beta}\nabla\varepsilon_\alpha + i\boldsymbol{\mathcal{A}}_{\alpha\beta}(\varepsilon_\alpha - \varepsilon_\beta), \tag{B69}$$

where $\boldsymbol{\mathcal{A}}_{\alpha\beta} \equiv i\langle\psi_\alpha|\nabla\psi_\beta\rangle$. Combining Eqs. (B67)-(B69), we hence find

$$\mathrm{Tr}[\nabla\hat{H}\hat{\rho}] = \sum_\alpha \rho_\alpha \nabla\varepsilon_\alpha + i\sum_{\alpha\beta}(\rho_\alpha - \rho_\beta)\boldsymbol{\mathcal{A}}_{\alpha\beta}\mathcal{M}_{\beta\alpha} + \mathcal{O}\left(\lambda^2 v_\mathrm{F}\right) \tag{B70}$$

We identify the first term in the right-hand side above as the contribution arising from the group velocity.

To rewrite the second term, we use that $|\partial_t\psi_\alpha\rangle = \frac{e}{\hbar}\mathbf{E}\cdot|\nabla\psi_\alpha\rangle$, implying $\mathcal{M}_{\alpha\beta} = \frac{e}{\hbar}\mathbf{E}\cdot\boldsymbol{\mathcal{A}}_{\alpha\beta}$ [81]. Thus

$$\sum_{\alpha\beta}(\rho_\alpha - \rho_\beta)\mathcal{M}_{\alpha\beta}\mathcal{A}^j_{\beta\alpha} = \frac{e}{\hbar}\sum_{\alpha\beta,i}(\rho_\alpha - \rho_\beta)E_i\mathcal{A}^i_{\alpha\beta}\mathcal{A}^j_{\beta\alpha} \tag{B71}$$

where $\mathcal{A}^i_{\alpha\beta}$ and E_i denotes the ith vector component of $\boldsymbol{\mathcal{A}}_{\alpha\beta}$ and $\mathbf{E}$, respectively. Next, we note

$$\sum_{\alpha\beta}(\rho_\alpha - \rho_\beta)\mathcal{A}^i_{\alpha\beta}\mathcal{A}^j_{\beta\alpha} = \sum_{\alpha\beta}\rho_\alpha(\mathcal{A}^i_{\alpha\beta}\mathcal{A}^j_{\beta\alpha} - \mathcal{A}^j_{\alpha\beta}\mathcal{A}^i_{\beta\alpha}) \tag{B72}$$

Using the definition of $\mathcal{A}^i_{\alpha\beta}$ along with $\langle\psi_\alpha|\partial_i\psi_\beta\rangle = -\langle\partial_i\psi_\alpha|\psi_\beta\rangle$, we find $\sum_\beta \mathcal{A}^i_{\alpha\beta}\mathcal{A}^j_{\beta\alpha} = \langle\partial_i\psi_\alpha|\partial_j\psi_\alpha\rangle$. Hence

$$\sum_{\alpha\beta}(\rho_\alpha - \rho_\beta)\mathcal{A}^i_{\alpha\beta}\mathcal{A}^j_{\beta\alpha} = \sum_\alpha \rho_\alpha(\langle\partial_i\psi_\alpha|\partial_j\psi_\alpha\rangle - \langle\partial_j\psi_\alpha|\partial_i\psi_\alpha\rangle) \tag{B73}$$

We identify the right-hand side as $-i\sum_{\alpha,k}\rho_\alpha\epsilon_{ijk}\Omega^k_\alpha$, where ϵ_{ijk} denotes the Levi-Civita tensor and Ω^k_α denotes the kth component of $\boldsymbol{\Omega}_\alpha$. Thus,

$$\sum_{\alpha\beta}(\rho_\alpha - \rho_\beta)\boldsymbol{\mathcal{A}}_{\alpha\beta}\mathcal{M}_{\beta\alpha} = -i\frac{e}{\hbar}\sum_\alpha \rho_\alpha \mathbf{E}\times\boldsymbol{\Omega}_\alpha \tag{B74}$$

Hence the second term in Eq. (B70) gives the contribution to the particle velocity from the anomalous velocity. In particular, by inserting the above result into Eq. (B70), and dividing through with $\hbar$, we establish Eq. (B66), which was the goal of this subsection.

5. Derivation of auxiliary results

In this subsection we derive the auxiliary results which we quoted in the subsections above. Specifically, we derive Eqs. (B9), (B10), and (B21). These results are established in Secs. B 5 c, B 5 a, and B 5 b, respectively.

a. *Near-stationarity of ρ_α [Eq. (B9)]*

We first show that ρ_α is nearly stationary.

Our starting point is the equation of motion for the diagonal matrix elements of $\hat{\rho}(\mathbf{k},t)$ in the orbital basis, $\{f_{\boldsymbol{n}}(\mathbf{k},t)\}$, $\partial_t f_{\boldsymbol{n}}(t) = -\sum_k R^{\boldsymbol{mm}}_{\boldsymbol{nn}}(t)f_{\boldsymbol{m}}(t)$. We note that $R^{\boldsymbol{mm}}_{\boldsymbol{nn}}(\mathbf{k},t)$ is of order Γ, but oscillates with characteristic frequency Ω. As a result, we expect $f_{\boldsymbol{n}}(\mathbf{k},t)$ to deviate from its time-average, $\bar{f}_{\boldsymbol{n}}(\mathbf{k})$, by a correction of order Γ/Ω:

$$f_i(\mathbf{k},t) = \bar{f}_i(\mathbf{k}) + \mathcal{O}(\lambda). \tag{B75}$$

Inserting this into Eq. (B58), we thus find

$$\rho_\alpha = \bar{\rho}_\alpha + \mathcal{O}(\lambda). \tag{B76}$$

where $\bar{\rho}_\alpha(\mathbf{k})$ denotes the time-average of $\rho_\alpha(\mathbf{k},t)$, and we neglected a correction of order λ^2, since it is subleading relative to Γ/Ω.

b. *Bounds on group velocity [Eq. (B10)]*

We next establish the bounds on the group velocity in Eq. (B10). To obtain this result, we note that $\frac{1}{\hbar}|\nabla\varepsilon_\alpha| = \frac{1}{\hbar}|\langle\psi_\alpha|\nabla H|\psi_\alpha\rangle| \leq v_\mathrm{F}$. This establishes the first condition in Eq. (B10).

To establish the second condition in Eq. (B10), we use that

$$\frac{e}{\hbar}\mathbf{E}(t)\times\boldsymbol{\Omega}_\alpha(t) = i\sum_\beta(\boldsymbol{\mathcal{A}}_{\alpha\beta}\mathcal{M}_{\beta\alpha} - \boldsymbol{\mathcal{A}}_{\beta\alpha}\mathcal{M}_{\alpha\beta}) \tag{B77}$$

This follows from Eq. (B74) after setting ρ_α equal to 1 for one particular choice of α and 0 for all other choices. Next, we use that $|\boldsymbol{\mathcal{A}}_{\alpha\beta}| = |\langle\psi_\alpha|\nabla H|\psi_\beta\rangle/(\varepsilon_\alpha - \varepsilon_\beta)| \leq v_\mathrm{F}/\delta\varepsilon$. Since $|\mathcal{M}_{\alpha\beta}| \lesssim \lambda\delta\varepsilon$ [see Eq. (B28)], we thus conclude that $\frac{e}{\hbar}|\mathbf{E}(t)\times\boldsymbol{\Omega}_\alpha(t)| \lesssim \lambda v_\mathrm{F}$. This was what we aimed to show.

c. *Expression for $\hat{Q}_1(t)$ [Eq. (B21)]*

We finally prove that, for each α, the unitary operator in Eq. (B21),

$$\hat{Q}_1(t) = \mathcal{T}e^{-i\int_0^t dt'\sum_{\alpha\beta}\mathcal{M}_{\alpha\beta}(t')\hat{\psi}^\dagger_\alpha(t')\hat{\psi}_\beta(t')}\hat{V}_1, \tag{B78}$$

transforms the eigenmode of the Hamiltonian, $\hat{\psi}_\alpha(\mathbf{k},t)$ into the orbital annihilation operator $\hat{c}_\alpha$:

$$\hat{Q}^\dagger_1(t)\hat{\psi}_\alpha(t)\hat{Q}_1(t) = \hat{c}_\alpha, \tag{B79}$$

We first note that $\hat{Q}_1(t)$ is quadratic and conserves the number of fermions. Hence, $\hat{Q}^\dagger_1(t)\hat{\psi}_\alpha(t)\hat{Q}_1(t)$ must be a linear combination of the orbital annihilation operators:

$$\hat{Q}^\dagger_1(t)\hat{\psi}_\alpha(t)\hat{Q}_1(t) = \sum_i K_{\alpha i}(t)\hat{c}_i \tag{B80}$$

for some matrix $K_{\alpha i}(t)$. Eq. (B79) is satisfied if $K_{\alpha i}(t) = \delta_{\alpha i}$.

We can find $K_{\alpha i}(t)$ from the single-particle evolution of the system, using $|i\rangle = \hat{c}^\dagger_i|0\rangle$ and $|\psi_\alpha(t)\rangle = \hat{\psi}^\dagger_\alpha(t)|0\rangle$:

$$K_{\alpha i}(t) = \langle\psi_\alpha(t)|Q_1(t)|i\rangle, \tag{B81}$$

where $Q_1(t)$ is the operator $\hat{Q}_1(t)$ projected into the single-particle space:

$$Q_1(t) = \mathcal{T} e^{-i\int_0^t ds \sum_{\alpha\beta} |\psi_\alpha(s)\rangle\langle\psi_\beta(s)| \mathcal{M}_{\alpha\beta}(s)} e^{\sum_{ij} |i\rangle\langle j| \log(M)_{ij}}. \tag{B82}$$

Since $M_{ij} = \langle i|\psi_j(0)\rangle$, we find

$$e^{\sum_{ij} |i\rangle\langle j| \log(M)_{ij}} = \sum_{ij} |i\rangle\langle j| M_{ij} \tag{B83}$$

Using $\sum_{ij} |i\rangle\langle j| M_{ij} = \sum_i |\psi_i(0)\rangle\langle i|$, we find

$$K_{\alpha i}(t) = \langle\psi_\alpha(t)| \mathcal{T} e^{-i\int_0^t ds \sum_{ij} \mathcal{M}_{ij}(s) |\psi_i(s)\rangle\langle\psi_j(s)|} |\psi_i(0)\rangle, \tag{B84}$$

implying

$$K_{\alpha i}(0) = \delta_{\alpha i}. \tag{B85}$$

To see that $K_{\alpha i}(t)$ also equals $\delta_{\alpha i}$ at later times, we take the time-derivative above:

$$\partial_t K_{\alpha i}(t) = \Big(\langle \partial_t \psi_\alpha(t)| - i \sum_\beta \mathcal{A}_{\alpha\beta}(t) \langle\psi_\beta(t)| \Big) Q_1(t) |i\rangle \tag{B86}$$

Since $\langle\psi_\alpha(t)|\partial_t\psi_\beta(t)\rangle = -\langle\partial_t\psi_\alpha(t)|\psi_\beta(t)\rangle$, $\mathcal{M}_{\alpha\beta}(t) = -i\langle\partial_t\psi_\alpha(t)|\psi_\beta(t)\rangle$. This result, along with $\sum_\beta |\psi_\beta(t)\rangle\langle\psi_\beta(t)| = 1$, implies

$$\sum_\beta \mathcal{M}_{\alpha\beta}(t) \langle\psi_\beta(t)| = -i \langle \partial_t \psi_\alpha(t)|. \tag{B87}$$

Using this in Eq. (B86), we conclude that $\partial_t K_{\alpha i}(t) = 0$. Since we found above that $K_{\alpha\beta}(0) = \delta_{\alpha\beta}$, it hence follows that

$$K_{\alpha i}(t) = \delta_{\alpha i} \tag{B88}$$

at all times t. Using this result in Eq. (B80), we conclude that Eq. (B79) holds. This was what we wanted to show, and concludes this appendix.

Appendix C: Derivation of bound on d_0

Here we derive the condition for adiabaticity which we quote above Eq. (36) and the text above. I.e., we seek to establish that the time-dependence of $H(\mathbf{k}, t)$ can be considered adiabatic for $\mathbf{k}$-points where

$$\min_t |\mathbf{k} + e\mathbf{A}(t)/\hbar| \gtrsim \sqrt{\frac{\|R\| eE}{\hbar v_0^2}}. \tag{C1}$$

See main text for definition of quantities and notation.

Our starting point is Eq. (35), which states that the dynamics of the system are adiabatic for $\mathbf{k}$-points where

$$\hbar \|\partial_t H(\mathbf{k} + e\mathbf{A}(t)/\hbar)\| \ll \delta\varepsilon^2(\mathbf{k} + e\mathbf{A}(t)/\hbar) \tag{C2}$$

for all t.

We consider the dynamics near a Weyl point, where the Hamiltonian takes the linearized form $H(\mathbf{k}) = \boldsymbol{\sigma} \cdot R\mathbf{k} + \mathbf{V} \cdot \mathbf{k}$ [see Eq. (1)]. We ignore the second term arising from the Weyl cone tilt $\mathbf{V}$, since it only affects the time evolution through an overall phase factor. With this linearized form we find

$$\delta\varepsilon(\mathbf{k}) = |R\mathbf{k}|, \tag{C3}$$

$$\hbar \|\partial_t H(\mathbf{k} + e\mathbf{A}(t)/\hbar)\| = e|R\mathbf{E}(t)| \tag{C4}$$

Thus dynamics in the system are adiabatic if

$$e|R\mathbf{E}(t)| \ll |R(\mathbf{k} + e\mathbf{A}(t)/\hbar)|^2 \tag{C5}$$

We now use that $|R\mathbf{E}(t)| \lesssim \|R\| E$, where E denotes the characteristic magnitude of the driving-induced electric field. Moreover, $|R\mathbf{v}| \geq v_0 |\mathbf{v}|$ where v_0 denotes the smallest eigenvalue of R. Combining these two inequalities with Condition (C5), we conclude that the time-dependence of the Hamiltonian is adiabatic if

$$\|R\| \frac{eE}{\hbar} \lesssim v_0^2 |\mathbf{k} + e\mathbf{A}(t)/\hbar|^2 \tag{C6}$$

for all t.

Rearranging the factors above, we conclude that the dynamics of the system are adiabatic if Condition (C1) is satisfies. This was what we wanted to show.